A Study on the Charging Mechanisms of Electrically Insulated Substrates in Negative-Ion Implantation

Yoshitaka TOYOTA

January 1996

Abstract

Conventional positive-ion implantation into the insulating or the insulated materials is accompanied with a charging problem owing to charge transportation to the implanted target. In contrast, negative-ion implantation can be expected to be quite effective for charging-free implantation because of being intrinsically less prone to charging, unlike positive-ion implantation. This study focuses on the charging mechanisms of the insulating and the insulated materials in negative-ion implantation.

The charging during negative-ion implantation is related closely to secondary electrons emitted from the surface because the magnitude of the secondary-electron current is comparable to or larger than that of the negative-ion current. Accordingly, it was assumed that the charging mechanisms of the insulating or the insulated materials during negative-ion implantation are linked with the yield and the energy distribution of secondary electrons. Thus, this study is divided into two main parts; one is on secondary electron emission induced by negative ions, and the other is on the charging mechanisms of the insulating or the insulated materials during negative-ion implantation.

A discussion on secondary electron emission induced by negative ions is made on the basis of the yield and the energy distribution of secondary electrons measured for the conductive and the insulating materials. This is the first summary on the yield and the energy distribution of secondary electrons induced by negative ions. The measured data have indicated the same properties and the same basic emission mechanisms irrespective of the conductivity of the target materials. In addition, it has been discovered that the negative-ion-induced secondary electrons consists of an extra electron released from a negative ion in ion impact on a solid surface and the electrons originating from kinetic emission.

Another discussion on the charging mechanism during negative-ion implantation is made, related to the measured data of the negative-ion-induced secondary electrons. The charging mechanism during negative-ion implantation was studied on the insulating or the insulated materials, respectively. The experimental results and theoretical consideration is as follows: (a) the isolated electrode during negative-ion implantation is positively charged and its charging voltage is as low as several volts. Taking into account the behavior of the emitted secondary electrons, an equilibrium charging-voltage equation expressed only by the yield and the energy distribution was presented. As a consequence, it has been revealed that the low equilibrium-charging of the isolated electrodes in negative-ion implantation is achieved owing to the low-energy secondary electrons pulled back to the electrode. In addition, it has been demonstrated that the slope of the energy distribution extending toward the high-energy region determines that the charging voltage is proportional to the yield. (b) The charging of the insulating materials during negative-ion implantation was examined by secondary-electron energy analysis. As a result, it has been found out that the charging voltage is negative and its absolute value increases almost in proportion to the yield of secondary electrons. To examine the negative charging of the insulating materials during negative-ion implantation, a simplified charging model based on an electric double layer was proposed. This model explained the charging properties qualitatively. It has been predicted that the low equilibrium-charging of the insulating materials in negative-ion implantation is achieved owing to the electric double layer playing a role of a gate to make the yield equal to one.

This study has demonstrated an intimate relationship between the emitted secondary electrons and the charging of the insulating or the insulated materials during negative-ion implantation. In conclusion, it has been verified that the negative-ion implantation is inherently less prone to charging.

Acknowledgments

I am deeply indebted to Professor Junzo Ishikawa of Kyoto University for providing me the opportunity to study on negative-ion implantation and for his continuous guidance and encouragement throughout this study. I also wish to thank Professor Kunihide Tachibana of Kyoto University and Professor Nobutsugu Imanishi of Kyoto University for a critical reading of the manuscript and helpful suggestions and observations.

I wish to express my sincere appreciation to Professor Ryuji Koga for his guidance and advice at Okayama University and recommending me for the study at Ishikawa Laboratory. I am also grateful to Associate Professor Osami Wada for frequent, stimulating, and invaluable discussions in my research days at Okayama University.

I would like to thank Research Associate Hiroshi Tsuji for fruitful discussions and his considerable assistance in accomplishing this work. I would like to express my gratitude to Research Associate Yasuhito Gotoh for many helpful suggestions and valuable comments on earlier drafts of this dissertation.

Thanks are due to the members of Ishikawa Laboratory, especially the members of Ion Sources Research Laboratory, Messrs. Shoji Nagumo, Chikara Ichihara, Hirofumi Honda, Shigeo Ikeda, and Yoshiji Matsuda, who carried out much of the experimental work. It is a pleasure to thank Mr. Shigeki Sakai for providing the instruments and samples.

I am thankful to Messrs. Steve Burkholder and Kazuto Sateau for the English correction of this dissertation. I would like to acknowledge the heartfelt encouragement of Miss Yuka Tatsumi.

Finally, I would like to thank all those involved in this study. In particular, I am much indebted to my parents and grandmother for their constant encouragement and support.

List of Symbols

The following list contains the symbols used in the doctoral dissertation.

Symbol	*Quantity*
a	ion-beam radius
a_0	Bohr radius; a_0=0.0529 nm
A, A', B, C	dimensionless functions of the yield, γ, and the dimensionless parameter, α
d	thickness of the insulating material
d_{acc}	aperture diameter of the accelerator; d_{acc}/l_{ret} denoting the aspect ratio
D, D_p	parameter in the transferred energy function
D_s	distance between the insulating surface and the shield
e	electronic charge
E	electron energy
E_F	Fermi level
E_i	ionization energy
$E_t(z)$	electronic transferred energy originating from both projectile and recoil atoms
E_{t0}	maximum value of electronic transferred energy
E_{max}	maximum energy of secondary electrons
E_p	most probable energy of $N_c(E)$
E_s	energy of an impinging ion
E_z	energy of an impinging ion at a depth of z from the surface
I_0	incident-ion current
I_{cc}	charge-compensation current
$I_{sc}(V_{ret})$	signal current detected by sweeping the retarding voltage, V_{ret}
I_{sc}^*	current detected at V_{ret}=0 V; $I_{sc}^* = I_{sc}(0) < 0$

I_{se}	secondary-electron current
J	mean energy for the formation of an electron-hole pair
J_{ion}	ion current density
K	slope of the yield to the ion moment
l_{ret}	the retarding region length between the accelerator and the retarding electrode
L	mean attenuation length; $\exp(-z/L)$ denoting the attenuation function
L_p	length of the path which negative ions penetrate
m	mass of the monatomic ion
M	atomic weight of incident ion
n	density of the material
N^-	amount of negative ions after penetrating by the path length
N_0^-	initial amount of negative ions
$N(E)$	energy distribution of secondary electrons
N_c	energy distribution of secondary electrons from the insulating material in the charge equilibrium
N_d	number of the incident ion density per a second
$N_{ex}(z)$	number of the excited electrons, $N_{ex} = N_d E_t(z)/J$
$N'_{ex}(z)$	number of the excited electrons after scattering
p	ion momentum; $p = mv$
P	average escape probability for excited electrons into the vacuum
S_e	electronic stopping power for incident energy (constant)
$S_e(z, E_z)$	electronic stopping power at a depth of z from the surface for an impinging ion with an energy of E_z
t	implantation time
U	potential energy
v	ion velocity
v_0	Bohr velocity; $v_0 = 2.2 \times 10^6$ m·s^{-1}
V	charging voltage
V_{acc}	acceleration voltage

V_{bias}	voltage applied to an isolated electrode for verifying the measurement principle of secondary-electron energy analysis
V_c	charging voltage
V_c'	charging voltage measured by the voltmeter
V_{ext}	voltage applied to the collector for extracting secondary electrons
V_{ret}	retarding voltage
V_{sup}	voltage applied to the suppressor
z	depth from the surface
Z_1	projectile atomic number
Z_2	target atomic number
α	dimensionless function of the ion-beam diameter, $2a$, and the thickness of the insulating material, d, $\alpha = 1 - 2d/\sqrt{a^2 + (2d)^2}$
γ	yield of secondary electrons, $\gamma = \|I_{se}/I_0\|$
γ_0	intercept of the line representing the relationship between the yield and the ion momentum in negative-ion irradiation; $\gamma_0 \simeq 1$
γ_a	yield of secondary electrons for monatomic ions
γ_{C^-}	yield of secondary electrons for monatomic carbon ions
$\gamma_{C_2^-}$	yield of secondary electrons for diatomic carbon ions
γ_p	yield of secondary electrons for polyatomic ions
ΔE	energy deviation in the energy analyzer; $\Delta E/E$ denoting the energy resolution.
ε_0	permittivity in a vacuum
ε_r	relative permittivity of the insulating material
θ_{se}	angle of incidence on the energy analyzer
Λ	ratio of the yield to the electronic stopping power, $\Lambda = \gamma/S_e$
Λ_p	ratio of the yield to the ion moment, $\Lambda_p = \gamma/p$
Λ_v	ratio of the yield to the ion velocity, $\Lambda_v = \gamma/v$
ξ_e	parameter in the formula between the electronic stopping power and the incident ion, $\xi_e \simeq Z_1^{1/6}$
$\rho(z)$	charge density after the excited-electron redistribution

σ_{-10} single-electron detachment cross section

ϕ_{bp} beam potential at the beam center due to space charge of ion beam

ϕ_{col} work function of the collector made of stainless steel, $\phi_{col} = \phi_{sh}$

ϕ_{ret} work function of the mesh made of gold-evaporated tungsten wire which is attached to the retarding electrode

ϕ_s surface potential

ϕ_{sh} work function of the shield made of stainless steel

ϕ_{sp} work function of the isolated-electrode material

Contents

Abstract i

Acknowledgments iii

List of Symbols v

1 Introduction 1

1.1 Ion implantation in semiconductor fabrication 1

1.2 Negative-ion implantation 5

1.3 Research objectives 10

2 Negative-Ion-Induced Secondary Electrons 13

2.1 Introduction 13

2.2 Secondary-electron emission phenomenon 14

2.3 Yield measurement 20

2.3.1 Negative-ion implanter 20

2.3.2 Measurement apparatus 22

2.3.3 Results for conductive materials 24

2.3.4 Results for insulating materials 32

2.3.5 Comparison with positive-ion-induced secondary electrons 38

2.4 Energy distribution measurement 38

2.4.1 Measurement apparatus and method 38

2.4.2 Results for conductive materials 47

2.4.3 Results for insulating materials 52

2.5 Discussion 56

2.6 Summary 59

3 The Charging Mechanism of Isolated Electrodes in Negative-ion implantation **61**

3.1 Introduction 61

3.2 Charging voltage measurement 62

3.2.1 Measurement apparatus 62

3.2.2 Results of measurement 64

3.2.3 Comparison with positive-ion-implanted isolated electrodes 71

3.3 Modelling of negative-ion-implanted isolated electrodes 73

3.3.1 Equilibrium charging-voltage equation 73

3.3.2 Charging model evaluation 75

3.4 Discussion 78

3.5 Summary 83

4 The Charging Mechanism of Insulating Materials in Negative-Ion Implantation **87**

4.1 Introduction 87

4.2 Charging voltage estimation by secondary electron energy analysis 88

4.2.1 Measurement principle 88

4.2.2 Verification of measurement principle 90

4.3 Charging voltage during negative-ion implantation 93

4.4 Modelling of negative-ion-implanted insulating materials 99

4.4.1 Charging model based upon electrical double layer 99

4.4.2 Charging model evaluation 105

4.5 Discussion 105

4.6 Summary 113

5 Conclusions **115**

References **119**

List of Publications **125**

Chapter 1

Introduction

1.1 Ion implantation in semiconductor fabrication

It was in the late 1940s that Ohl *et al.* at Bell Labs first used ions to modify the electrical properties of silicon. They implanted positive helium ions into silicon single crystals to modify silicon rectifiers[1]. This is the first case of ion doping of silicon[2-4]. Around 1954, the patents on p-n junction formation using ion implantation began to be applied by Schockley[5,6], Ohl[7], and Mayer *et al.*[8] After that, Freeman developed a very useful ion source by 1962[9], and then the high current implanters based on this technology were established. As a result, a study on ion implantation technology of impurity doping began for industrial applications, and by the early 1970s the basic range calculations and anneal processes were understood; by 1975 implanters were being used as doping tools.

Ion implantation is a method of introducing ions accelerated at a few kV to a few MV into a solid to modify the properties of the material. For semiconductor single crystals, ion implantation has been utilized to introduce the impurities. The high-energy ions enter the crystal lattice, collide with the target atoms, and finally come to rest in the target. Ion implantation is a non-thermal process and hence the nuclear scattering events result in displaced target atoms. With increasing dose the individual regions of damage merge together and with a sufficiently large dose the target material becomes amorphous. In as-implanted semiconductor substrate, only a small number of ions will occupy substitutional sites and hence a large bulk of the ions is electrically inactive. To make the ions active, therefore, it is necessary to anneal the substrate by applying heat for an appropriate time. Simultaneously, annealing removes the damage due to the nuclear events.

The ion implanter is now an essential piece of equipment for the majority of semiconductor manufacturers. Figure 1.1 illustrates an example of the ion implantation process, i.e., source-drain (n^+ region) formation to the n-channel metal-oxide-semiconductor (MOS) region by arsenic-ion implantation into complimentary MOS (CMOS) circuit[10]. Nowadays, we need 20 implantation processes per wafer for 64 Mbits[2]. This frequent use of ion implantation in the semiconductor-fabrication process derives from the following advantages[3,4]: (a) It is possible to control the number and the distribution of implanted impurity atoms accurately by adjusting the acceleration voltage, ion current, and implantation time. This control allows concentration levels from 10^{14} to 10^{20} atoms$\cdot$cm^{-3} to be obtained with considerable accuracy. Thus, we obtain a much improved profile with a more abrupt change of concentration and more shrinking device dimensions. (b) Only one species is selected from the many ions produced in the plasma by an analyzing magnet. This selection enables to improve the purity of the impurities. (c) Previously implanted or diffused impurities are unaffected because of a room-temperature process, unlike high-temperature diffusions. In addition, rapid thermal annealing with laser beams in seconds and at relatively low temperature of 800 °C can be achieved with very little diffusion. (d) A much wider range of elements can be implanted in comparison with the number of elements which can be introduced by high-temperature diffusion. (e) The impurities can be implanted through a layer of oxide. This has important benefits for the manufacture of MOS circuits for gate voltage threshold adjustment. (f) Uniform doping to a large-area wafer can be performed with high reproducibility. (g) Ion implantation takes place in a vacuum and therefore is inherently clean. (h) The automatic control is easily done.

All these factors contribute to the general acceptance of ion implantation as one of the most useful tools for the manufacture of very large scale integrated circuits (VLSI). As device dimensions diminish and junctions become shallower ($\leq$ 20 nm), the n- and p-regions are increasingly being formed by ion implantation rather than by high-temperature diffusion. The present trend that the gate oxides become even thinner predicts that ion implantation will be the only tool for impurity doping in future semiconductor fabrica-

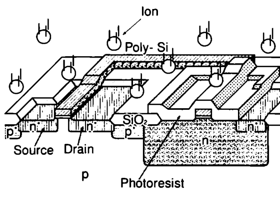

Figure 1.1 Schematic diagram illustrating source-drain formation to the n-channel MOS region in arsenic-ion implantation into CMOS circuit, deriving from ref. 10.

tion. Recently, ion implantation has been utilized not only in the large scale integrated circuit (LSI) and thin-film transistor (TFT) fabrication but also widely in the various fields such as surface modification of metals and insulating materials[11-20]. Besides this, there is also novel work of ion implantation into powders[21-23].

Ion implantation, however, has a significant problem: the charging of the insulating or insulated wafer surface. This is because, by its very nature, ion implantation transports charge to the implanted target. In addition, charging occurs not only because of the charges transported by the ions, but also because of the charges removed as secondary electrons due to ion bombardment. Hence, neutral-particle implantation also incurs the same charging problem as positive-ion implantation. Semiconductor implants frequently involve wafers with insulating and/or insulated surfaces. Charge buildup on the wafer surface during implantation affects device yield as follows[24-30]: excess charging beyond the breakdown voltage in such wafers produces microscopic craters, i.e., punch through craters; even wafer charging below the breakdown voltage can result in non-uniform implants[28]. Accordingly, it is quite important to solve the charging problem in semiconductor fabrication. The conventional implanter has an electron flooding or shower, designed to generate low energy electrons in the vicinity of the target, to neutralize positive charge-buildup[31,32]. However, the need for forced neutralization is not universal owing to the much stronger yield dependence on device structure and chip layout. Hence, it is extremely difficult to neutralize using such an external charge compensation system. For example, there can occur negative charging up to -50 V as a result of excess supply of electrons with a maximum energy of 50 eV. The charging voltage of 50 V is not necessarily low in semiconductor fabrication. As the gate oxide thicknesses decrease according to increased gate density and reduced junction depths, wafer surface neutralization using the above system becomes even more severe. At present, it is necessary to suppress the charging voltage within $\pm$ several volts so as not to affect device yield. Thus, the continuing trend toward thinner gate oxides does require a completely new method for charging-free implantation. Negative-ion implantation, treated in this study, is expected to be quite effective for charging-free implantation because of intrinsically low charging.

1.2 Negative-ion implantation

As already described, all the conventional implanters utilize positive ions. This is because it has long been believed that positive ions are more easily produced in comparison with negative ions and that, in contrast, it is considerably difficult to produce heavy negative ions for industrial applications, except for negative hydrogen ions. In fact, positive ions are easily extracted from positively biased plasma which is generated by collision with electrons and accompanying ionization. Although there exist quite a few negative ions in the plasma, it is difficult to extract only negative ions in the above manner because a lot of electrons in the plasma are extracted together. It was discovered, however, that the presence of minute amounts of an alkali metal, such as cesium, on a surface enhances the probability for negative-ion formation of particles ejected from the surface during sputtering[33]. The maximum negative-ion production probabilities are listed in Table 1.1, when the cesiated solid surface was sputtered by xenon ions[34, 35]. The probabilities are about 10% and approximately a hundred times as large as those without cesium coverage. Thus, secondary negative-ion emission by sputtering can be used as an ion-production method to obtain various high-current heavy negative-ion beams.

The first heavy negative-ion source, to which the secondary negative-ion emission was applied, was constructed by Mueller and Hortig in 1969[36]. In those days, however, the mechanism of heavy negative-ion production did not attract researcher's notice.

Table 1.1 Maximum negative-ion production probabilities in secondary negative-ion emission due to sputtering each cesiated solid surface by xenon ions[34, 35].

	Ion species				
	C^-	Si^-	Cu^-	Ge^-	W^-
Production probability (%)	18.3	15.6	12.1	13.6	8.1

Hence, heavy negative-ion sources had been developed for tandem accelerators which need a number of negative-ion species rather than a large amount of negative-ion current: in the 1970s, the universal negative-ion source (UNIS)[37] and Aarhus negative-ion source (ANIS)[38] delivered a few tens of microamperes of various heavy negative-ion beams; in the early 1980s, the versatile high intensity negative-ion source[39] delivered a few hundreds of microamperes; at the end of 1980s, a bucket-type plasma-sputter heavy negative-ion source[40] delivered several milliamperes in pulse mode. For industrial applications of negative-ion implantation, neutral and ionized alkaline metal bombardment-type heavy negative-ion source (NIABNIS)[41-43] and rf-plasma-sputter-type heavy negative-ion source[34,44,45] were developed. In particular, the latter, designed under the concepts of a large sputtering target surface, uniform sputtering by plasma ions, a precise cesium supply to the sputtering target, temperature control of the sputtering target, and a low gas pressure discharge, extracted the order of milliamperes of negative-ion beams in dc mode. Table 1.2 summarizes the maximum dc negative-ion currents measured just after the extraction electrode[35], indicating the order of milliamperes of negative-ion currents sufficient for negative-ion implantation into semiconductors. Besides, the depth profile of carbon atoms implanted into a silicon substrate at 50 keV with a dose of 1×10^{17} ions·cm^{-2}, which was quantitatively analyzed by Auger electron spectrometry (AES), and a theoretical curve calculated by the LSS theory[46] agreed well with each other[47]. This indicates that the depth profile can be controlled by adjusting the

Table 1.2 Maximum dc negative-ion currents extracted from rf-plasma-sputter type heavy negative-ion source[35].

	Ion species					
	B_2^-	C^-	C_2^-	Si^-	P^-	Cu^-
Ion current (mA)	1.0	1.6	2.3	3.8	0.8	12.1

acceleration voltage in negative-ion implantation as well as in positive-ion implantation.

Negative-ion implantation has another remarkable property. Figure 1.2 shows the depth profile of carbon atoms implanted at 20 keV into a silicon dioxide sheet with a dose of 1×10^{16} ions·cm^{-2} without any charge neutralization[35]. The profile, measured by secondary ion mass spectrometry (SIMS), also agreed well with a LSS curve[46] in spite of insulating material. The carbon concentration which is steady at about 10^{20} atoms·cm^{-3} in the deeper region than the most probable concentration is due to detection of a high dose of carbon surrounding the measured point, not due to diffusion. The agreement of the depth profile suggests that negative-ion implantation is intrinsically less prone to charging, because the surface charging apparently reduces the incident energy and hence the implantation depth should be shallower than that in theory. The figure also indicates no cesium contamination although cesium vapor was used in the negative-ion source. No contamination is very important in semiconductor fabrication. Furthermore, the charging voltage of electrically insulated aluminum bombarded by positive- and negative-carbon ions as a function of dose[48] is shown in Fig. 1.3. No charge neutralization was carried out in this measurement, either. The charging voltage in positive-ion bombardment increases in proportion to the ion dose. This suggests that positive-ion implantation into the electrically insulated material without charge neutralization is equivalent to a charge supply to a capacitor. On the other hand, the charging voltage during negative-ion implantation increases slowly with the ion dose and approaches to a certain value. The low charging in negative-ion implantation is considered to be caused by incident negative ions compensating secondary electrons moving away from the target surface in ion bombardment. Thus, no breakdown of insulating materials is expected in negative-ion implantation.

To utilize negative-ion implantation as a charging-free implantation method, it is necessary to understand the charging phenomenon. It can be considered that the charging during negative-ion implantation is related closely to secondary electrons emitted from the target, because the amount of the secondary electrons and incident ions are of almost the same order. To examine the inherently low charging during negative-ion implantation, therefore, it is also important to investigate the behavior of secondary electrons.

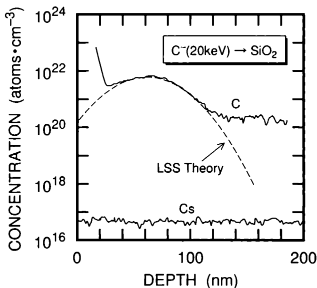

Figure 1.2 Depth profile of implanted carbon atoms in negative-carbon-ion implantation into a silicon dioxide substrate at an energy of 20 keV with a dose of 1×10^{16} ions·cm^{-2} without any charge neutralizaion[35]. The cesium atom signal consists in the noise level.

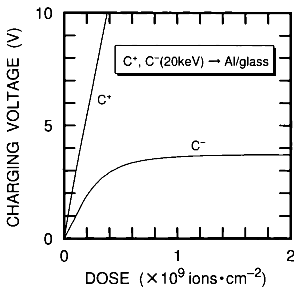

Figure 1.3 Charging voltage of electrically insulated aluminum bombarded by positive- and negative-carbon ions without any charge neutralization as a function of dose[48].

1.3 Research objectives

Ion implantation is a very useful technique for modifying the properties of materials. Thus, ion implantation will be applied much more widely to the various fields in the future. In semiconductor fabrication also, ion implantation will play an increasingly significant role as device dimensions diminish and junctions become shallower. However, conventional positive-ion implantation has a serious problem of wafer charging, because the charging brings the non-uniform implants and dielectric breakdown and hence reduce device yield. The charging originates from positive-charge accumulation on the surface owing to positive charges transported by the incident ions. In addition, secondary electron emission caused by ion impact on the target enhances the wafer charging. Thus, the charging in positive-ion implantation into the electrically insulated material is inevitable. So far, an external neutralization system such as an electron flooding has managed to compensate the positive-charge buildup. However, the still thinner gate oxides in the future will make the external neutralizer useless. Contrary to positive-ion implantation, negative-ion implantation is intrinsically less prone to charging as observed in the preliminary experiment. This can be considered to be because the negative charges of the incident ions compensate the moving-away negative charges as a result of secondary electron emission. Thus, negative-ion implantation is expected to be quite effective for charging-free implantation.

This study focuses on the charging of the insulating and the insulated materials in negative-ion implantation. Although some preliminary experiments have indicated the low charging of the insulating and the insulated materials during negative-ion implantation, this benefit might not be applicable to every condition. In order to utilize the benefit of the low charging in negative-ion implantation, therefore, it is extremely important to understand the charging phenomenon in detail. It can be considered that the charging is related closely to secondary electrons emitted from the surface because the magnitude of the secondary-electron current is, in general, comparable to or larger than that of the negative-ion current. Accordingly, this study assumed that the charging mechanisms of the electrically insulated materials during negative-ion implantation are linked with the

yield and the energy distribution of secondary electrons. Therefore, there is another interest in secondary electrons induced by negative ions. Unfortunately, secondary electron emission induced by heavy negative ions has hardly been examined, and hence this study started with the measurement of the secondary electrons. As a consequence, this is the first summary on negative-ion-induced secondary electrons.

Figure 1.4 shows the flowchart of this doctoral dissertation. This dissertation is divided into two main parts: one is on negative-ion-induced secondary electron emission (Chapter 2), and the other is on the charging mechanisms of the insulating or the insulated materials during negative-ion implantation (Chapters 3 and 4). The charging mechanisms for both of the insulating and the insulated materials are discussed on the basis of the measured data of secondary electrons, namely, the yield and the energy distribution. Chapter 2 describes the yield and the energy distribution of secondary electrons emitted from the target surface in negative-ion implantation[49-52], where the conductive and the insulating materials are used as the target. A comparison with the results by positive-ion bombardment is made to clarify the properties of secondary electrons induced by negative ions. In Chapters 3 and 4, charging during negative-ion implantation is discussed, taking into account the measured data of secondary electrons obtained in Chapter 2. Chapter 3 deals with the charging of an electrically insulated conductive material, which is designated an isolated electrode in this study, during negative-ion implantation[35, 49, 53-56]. The dependence of the charging voltage on the various implantation conditions, such as ion velocity and ion species, is described. A charging model during negative-ion implantation is proposed to prove the low charging due to secondary-electron self-regulating. On the other hand, the charging of the negative-ion-implanted insulating materials is described in Chapter 4[35, 57-61]. The charging voltage is evaluated from the energy shift of the emitted secondary electrons by secondary-electron energy analysis because it is impossible to measure the charging voltage directly. Furthermore, another charging model based on an electric double layer for the negative-ion-implanted insulating materials is proposed to explain the charging of the insulating materials. Finally, the summary of this study is given in Chapter 5.

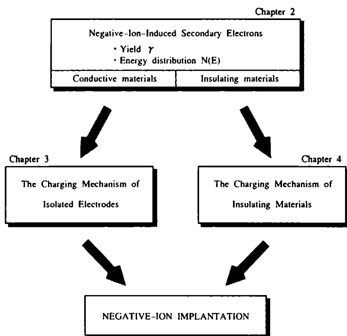

Figure 1.4 Flowchart of this doctoral dissertation and the theme in each chapter.

Chapter 2

Negative-Ion-Induced Secondary Electrons

2.1 Introduction

Under suitable conditions, ions striking a surface cause electrons to be emitted. This phenomenon is well known as secondary electron emission[62, 63]. Besides the current resulting from secondary electrons, there exist currents resulting from charged particles, such as incident ions, backscattered ions, and secondary ions, and leakage current, flowing into or out of the target during ion implantation. The equilibrium charging voltage is determined when the sum of the currents apparently vanishes. The magnitude of the incident-ion current and the secondary-electron current is of almost the same order and relatively large compared with that of the currents due to the other charged particles. Hence, secondary electrons play a significant role for charging during ion implantation.

Secondary electron emission induced by electron bombardment has been treated in recent reviews[64-66]. In addition to these recent articles, secondary electron emission has been comprehensively discussed[67-70]. Recent reviews for positive-ion-induced secondary electron emission have been presented[71-73]. Thus, a large number of papers on secondary electron emission induced by electrons and positive ions has been reported. In contrast, there are few reports on secondary electron emission induced by heavy negative ions. Even if any, there must be considerable doubt as to the experimental data. For example, Hird *et al.*[74] compared the yield of secondary electrons between positive- and negative-ion impact on a stainless steel surface as for chlorine, iodine, and oxygen ions. However, the

effect of secondary electrons emitted from the grid was left and, moreover, the measured values are so scattered that no explicit tendency is observed. Even from this point of view, it is important to examine negative-ion-induced secondary electron emission.

The following information can be obtained from the measurements of ion-induced secondary electron emission: the yield, the energy distribution, the angular distribution, etc. The first two parameters, the yield and the energy distribution of secondary electrons, are treated in this chapter. The yield of secondary electrons, denoted by γ, is the average number of emitted electrons per incident ion. In practice, the yield of secondary electrons is defined as

$$\gamma = \left| \frac{I_{se}}{I_0} \right|, \tag{2.1}$$

where I_0 is the incident-ion current and I_{se} is the secondary-electron current. Equation (2.1) is represented by the absolute value, taking into account the positive- and negative-ion-current flows in the opposite direction. On the other hand, the energy distribution of secondary electrons is expressed by $N(E)$.

In this chapter, the secondary electron emission induced by negative ions is described in view of the experimental results, i.e. the yield and the energy distribution of secondary electrons emitted from the conductive and the insulating materials during negative-ion irradiation[49-52]. In addition, the features of the negative-ion-induced secondary electron emission are discussed in comparison with those of the positive-ion-induced secondary electron emission. In advance of the discussion on negative-ion-induced secondary electrons, a general explanation of secondary-electron emission phenomenon induced by positive ions, especially kinetic electron emission, is given.

2.2 Secondary-electron emission phenomenon

Secondary electron emission from a solid surface is a fundamental phenomenon which may happen whenever energetic charged particles or photons impinge on the surface. In addition, the emission of secondary electrons is a consequence of the interaction between the primary and recoil particles and the electrons in the solid, as shown in Fig. 2.1. The

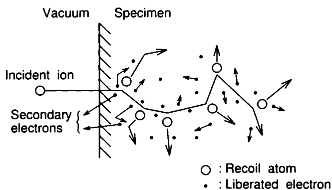

Figure 2.1 Schematic trajectories of charged particles in ion impact and secondary electron emission.

main fraction of emitted electrons originates from excitation of conduction electrons in metallic systems or from ionization processes in insulators.

Conventionally, positive-ion-induced secondary electron emission is divided into potential and kinetic emission. Potential emission[75,76] is associated with the neutralization of the impinging ions before they reach the surface and is, therefore, rather independent of the ion energy so far as the ion velocity is lower than the relevant atomic electron velocities[75]. The escaping electrons originate from a process of Auger neutralization in which the interaction of two conduction electrons causes one electron to neutralize the incident ion in the ground state and the other to be excited into the continuum above the filled band. As a result, potential emission will occur if the neutralization energy of the positive ion, namely, ionization potential, exceeds twice the work function of the target[75]. The yield based on potential emission is determined by the probability that these excited electrons can escape from the material, and therefore is 0.1 or lower[76]. The magnitude of this yield is estimated fairly accurately at low ion impact velocities by using a model developed by Kishinevskii[77]. In negative-ion bombardment, on the contrary, potential emission never occurs because negative ions are not neutralized by giving electrons.

Kinetic emission is, on the other hand, caused by ionizing collisions taking place inside the target, and hence depends on a large number of parameters: (a) for primary particles, incident energy, atomic number, mass and composition (*e.g.*, X_2^+ or XY^+), dose, and angle of incidence; (b) for targets, atomic number, mass and composition, structure, surface coverage and surface structure, and temperature. The absolute magnitude of the yield was evaluated by Sternglass[78] for higher ion velocities. For incident ions of low velocities, Parilis and Kishinevskii[79] developed a theory which predicts the yield from metals on the basis of Auger recombination processes as follows. For incident ions with an energy in the keV region or more, a cascade of recoiling target atoms may be generated. The incident ions and moving recoil atoms, in turn, may generate excited electrons by excitation of conduction electrons or ionization of valence electrons. Some liberated electrons may be able to reach the surface of the solid. Eventually, a certain fraction will escape from the

surface. This refers to the so-called three step model: generation, moving to the surface, and escape for the excited electrons[62,80]. It is well known[68] that secondary electrons originate mainly from a layer of the order of 0.5 2 nm below the surface in the case of metals and somewhat deeper in the case of semiconductors and insulators. This is because less conduction electrons extend the mean free path of excited electrons.

Baragiola *et al.*[81] proposed an expression for the yield from perpendicularly bombarded metal surfaces, which contains elements of the Parilis-Kishinevskii theory as well as those by Sternglass,

$$\gamma = \frac{P}{2J}\int_0^{\infty} S_e(z, E_z)\exp\left(-\frac{z}{L}\right)dz, \tag{2.2}$$

deriving from the three step model described above. $S_e(z, E_z)/J$, $\exp(-z/L)$, and P correspond to generation, moving to the surface, and escape, respectively. J is the mean energy for the formation of an electron-hole pair, independent of the ion velocity. P is the average escape probability for the excited electrons into the vacuum, resulting from integration over all electron energies and angles of incidence. $S_e(z, E_z)$ is the electronic stopping power at a depth of z from the surface for an impinging ion with an energy of E_z. The term, $\exp(-z/L)$, is the attenuation function for the excited electrons from their place of origin in a thickness, dz, at z, where L is the mean attenuation length. At sufficiently high velocities, the projectiles will lose a very small fraction of their energy over the mean electron escape depth, so that the stopping power is regarded as constant with respect to z and equal to that for the incident energy. We can then take the stopping power outside the integral in eq. (2.2), and obtain the important conclusion of the direct proportionality of the yield, γ, to the electronic stopping power of the particles incident on the target, S_e:

$$\gamma = \Lambda S_e, \tag{2.3}$$

where Λ is a parameter depending on the properties of the material, and has the following relationship with the projectile atomic number, Z_1: $\Lambda \propto Z_1^{-0.2}$[82]. Rösler *et al.*[62] gave a detailed discussion for this relationship. In addition, eq. (2.3) was confirmed by some experimental studies[81-86]. Holmén *et al.*[83] indicated that Λ is constant for krypton-ion

impact on copper over the energy range of 40–400 keV; for xenon-ion impact on copper, 100–400 keV. The corresponding velocities are $3\text{–}10\times10^5\ \mathrm{m\cdot s^{-1}}$ and $4\text{–}8\times10^5\ \mathrm{m\cdot s^{-1}}$, respectively. Dr. Clouvas's research group has also reported that Λ is independent of the projectile velocity in the velocity range of $10^5\ \mathrm{m\cdot s^{-1}}$ order[82,85,86].

It is well known[46] that the formula between the electronic stopping power, S_e, and the incident ion velocity, v,

$$S_e = \frac{1}{4\pi\varepsilon_0}\xi_e \cdot 8\pi e^2 a_0 \frac{Z_1 Z_2}{(Z_1^{2/3} + Z_2^{2/3})^{3/2}} \frac{v}{v_0}, \tag{2.4}$$

holds when v is small compared to $Z_1^{2/3} v_0$, where ε_0, e, a_0, v_0, and Z_2 are permittivity in a vacuum, electronic charge, Bohr radius and velocity, and target atomic number, respectively. ξ_e is of the order of 1–2 but may vary with Z_1 approximately as $\xi_e \simeq Z_1^{1/6}$. With the aid of eq. (2.4), eq. (2.3) can be reduced to

$$\gamma = \Lambda_v v. \tag{2.5}$$

Λ_v is constant so far as Λ is constant. The above discussion suggests that eq. (2.5) holds in the velocity range of $10^5\ \mathrm{m\cdot s^{-1}}$ order. Furthermore, the yield proportionality to the ion momentum, p, is also true:

$$\gamma = \Lambda_p p. \tag{2.6}$$

In addition to the electronic stopping power, Beuhler and Friedman[87] considered the velocity independent form as well as the Thomas-Fermi velocity dependent form, taking into account the influence of the nuclear stopping power of the particles penetrating into the target. The conclusion is as follows. The influence of the nuclear stopping power increases with decreasing ion energy. However, in the energy range of more than 20 keV, at which the projected range is on the order of 50 nm or more, and under the assumption that the escaping electrons originate from the first five atomic layers of the target, the influence of the nuclear stopping power is negligible.

Finally, the features of kinetic electron emission are summarized[63,87]. As shown in Fig. 2.2, the dependence of the secondary-electron emission yield (SEE yield) on the incident ion velocity is as follows[63]. Just beyond the region lying close to the threshold

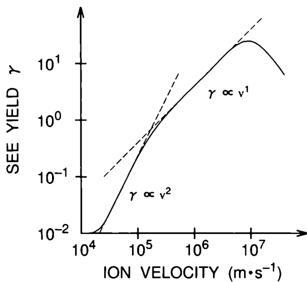

Figure 2.2 Example of the yield dependence on the ion velocity.

there exist the quadratic region ($\gamma \propto v^2$) and then the linear region ($\gamma \propto v$). The former extends approximately to 1.5–2×10^5 m·s^{-1}, and the latter begins immediately beyond the former and extends up to 2.5–3×10^6 m·s^{-1}. Beyond the maximum on the yield at 10^6–10^7 m·s^{-1} which corresponds to a region of a few tens, hundreds of keV, or even a few MeV, depending on ion species, a fall-off down to quite low values of the yield is observed. In addition to the velocity dependence, the additivity property of the yield[87], $\gamma_p = \sum \gamma_a$, is observed, where γ_a and γ_p denote the yield for monatomic and polyatomic ions at the same ion velocity, respectively. The sum is taken over all atoms of the polyatomic ions. This property describes that the polyatomic ions penetrate in the material separately. In the polyatomic ion made of the identical element, therefore, the dependence of the yield on the ion momentum gives the same curve irrespective of the atom number.

2.3 Yield measurement

2.3.1 Negative-ion implanter

Almost all experiments were carried out using a prototype negative-ion implanter. The implanter comprises a neutral and ionized alkaline metal bombardment-type heavy negative-ion source (NIABNIS)[41-43], a sector-magnet-type analyzing magnet, and an implantation chamber, as shown in Fig. 2.3(a). In the case of a graphite sputtering target, maximum negative-ion currents of 3.4 μA for negative carbon ions and 650 nA for negative dicarbon ions at an energy of 40 keV can be delivered to the implantation chamber. Figure 2.3(b) shows a typical mass spectrum of the negative-carbon-ion beam at the implantation chamber when cesium vapor was introduced. A few experiments requiring high ion current of more than a few μA were carried out by using another negative-ion source, rf-plasma-sputter-type heavy negative-ion source[34,44,45].

The ion-source chamber pumped by a 4 inch oil-diffusion pump with a liquid nitrogen trap was maintained at 10^{-4} Pa order during operation, because the negative-ion source is a sputter type without any gas feed. Not only the ion-source chamber but also the implantation chamber was pumped by oil-diffusion pumps with a liquid nitrogen trap

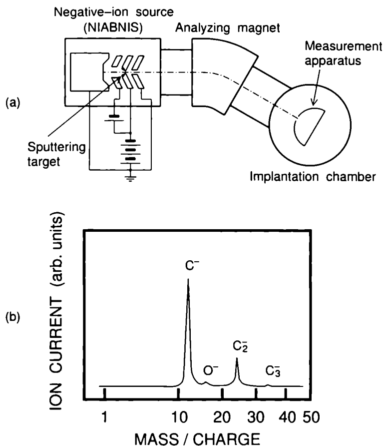

Figure 2.3 (a) Schematic diagram of a prototype negative-ion implanter equipped with a neutral and ionized alkaline metal bombardment type heavy negative-ion source (NIABNIS)[41-43], and (b) a typical mass spectrum of the negative-ion beam when using a graphite sputtering target.

and kept at 10^{-4} Pa order during implantation. In general, the yield and the energy distribution measurements of secondary electrons must be carried out under gas pressures of 10^{-8} Pa order or lower, and for a clean surface. This study assumes ion implantation in a semiconductor fabrication process. Thus, all experiments were carried out under the conditions of residual gas pressures of 10^{-4} Pa order and a dose of 10^{16} ions·cm^{-2}.

To reveal the properties of negative-ion implantation, positive-ion implantation was carried out in the same implanter as negative-ion implantation. In positive-ion implantation, an axial magnetic field extraction-type microwave ion source with a permanent magnet[88] was installed to the implanter shown in Fig. 2.3(a) instead of the NIABNIS. A positive-carbon-ion beam was extracted by feeding carbon dioxide gas as an ionization gas. Hence, the vacuum at the ion-source chamber was on the order of 10^{-3} Pa during operation, while the vacuum at the implantation chamber was still kept on the order of 10^{-4} Pa.

In each measurement of secondary electrons, the measurement apparatus was set in the implantation chamber so that a mass-separated positive- or negative-ion beam enters it, as shown in Fig. 2.3(a).

2.3.2 Measurement apparatus

Figure 2.4 shows the measurement apparatus for the yield of secondary electrons during negative-ion irradiation. The apparatus consists of a double hemispherical cup. During the measurement, the inner cup, or a collector was biased by +90 V to suppress the negative space-charge effect due to the emitted secondary electrons and detect all the secondary electrons emitted from the surface. On the other hand, the outer cup, or a shield was grounded in order not to count electrons in the vacuum chamber. An incident aperture of the outer cup, a limiter, is 8 mm in diameter. A suppressor, which is located between the limiter and the collector aligned along the beam line, was biased by −50 V to prevent the secondary electrons generated by ion impact on the limiter from entering the inner cup. The potential of the suppressor also prevents the secondary electrons due to ion impact on the specimen from going out of the inner cup.

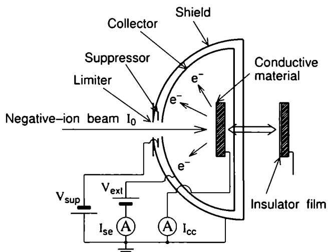

Figure 2.4 Schematic diagram of the measurement apparatus for the yield of secondary electrons.

The secondary-electron current, I_{se}, and the charge-compensation current, I_{cc}, can be simultaneously measured by using the apparatus shown in Fig. 2.4. Taking into account the sign in eq. (2.1), the yield for negative-ion irradiation is given by

$$\gamma = \frac{I_{se}}{I_0} = \frac{I_{se}}{I_{se} + I_{cc}}, \tag{2.7}$$

where I_0 is taken positive in entering the apparatus; both I_{se} and I_{cc} are positive in flowing to the ground. In negative-ion irradiation, hence, I_0 and I_{se} are both negative. Taking into account the sign in eq. (2.1), on the other hand, the yield for positive-ion irradiation appears as

$$\gamma = -\frac{I_{se}}{I_{se} + I_{cc}}. \tag{2.8}$$

In the yield measurement during irradiation onto the insulating material, a thin insulator film on a silicon substrate was mounted instead of the conductive material, as shown in Fig. 2.4.

2.3.3 Results for conductive materials

The yield of secondary electrons emitted from conductive materials during negative-ion irradiation was measured varying the following conditions: ion velocity, ion species, and ion current density. The experimental results obtained under each condition will be described below.

2.3.3.1 Ion velocity dependence

Figure 2.5 shows the dependence of the yield of secondary electrons on the ion velocity during negative-carbon-ion irradiation onto the conductive materials, such as platinum (closed circles), gold (closed diamonds), and aluminum (closed squares). The ion current density, depending on the ion velocity, was 9.7–410 nA·cm^{-2} for $C^- \to$ Pt; 0.56–120 nA·cm^{-2} for $C^- \to$ Au; 1.4–71 nA·cm^{-2} for $C^- \to$ Al. As described later, the secondary-electron emission yield is independent of the ion current density in the above ion-current-density range. Therefore, the feature shown in Fig. 2.5 reflects only the ion velocity dependence.

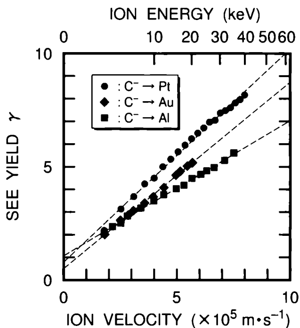

Figure 2.5 Dependence of the secondary-electron emission yield for negative-carbon-ion irradiation onto platinum, gold, and aluminum on ion velocity. The broken lines denote the results obtained from the least squares method.

The broken lines shown in Fig. 2.5 designate the results obtained by the least squares method. The yield increases in proportion to ion velocity in the ion velocity range of $2\ 8\times 10^5$ m·s^{-1}, implying that the main mechanism of secondary electron emission in negative-ion impact on the conductive material as well as that in positive-ion impact is kinetic emission[63]. In addition, the slope of the broken lines is different from one another. This indicates that the magnitude of the yield depends on the target materials. However, any intersection of the lines with the vertical axis is approximately one. This is not associated with the materials.

Equation (2.4) describes that the electronic stopping power increases with the target atomic number, Z_2. On the other hand, Λ depends on both of the projectile and the target. Hence, the dependence of the electronic stopping power on the target atomic number does not always coincide with the yield dependence, shown in Fig. 2.5. Nevertheless, the yield becomes large as the target atomic number is larger, when the difference between the two target atomic numbers is sufficiently large.

2.3.3.2 Ion species dependence

It was found out that the yield proportionality to ion velocity in the velocity range of $2\ 8\times 10^5$ m·s^{-1}, which is one of the significant features associating with kinetic emission, is true in negative-ion bombardment. Another feature, the additivity property of the yield, will be described in this section.

Figure 2.6 shows the yield of secondary electrons for monatomic ions (closed circles) and diatomic ions (closed squares) in negative-carbon-ion irradiation onto aluminum, as a function of ion velocity. Each broken line denotes the results obtained from the least squares method. Both intersections of the lines with the vertical axis at a velocity of 0 m·s^{-1} are approximately one. Now, let $\gamma_{C^-} = Kp + \gamma_0$, where both K and γ_0 are constants ($\gamma_0 \simeq 1$), and p is the ion momentum of the monatomic ion. The ion momentum is given by $p = mv$, where m and v are the mass and velocity of the monatomic ion, respectively. Assume that the negative polyatomic ions as well as the positive polyatomic

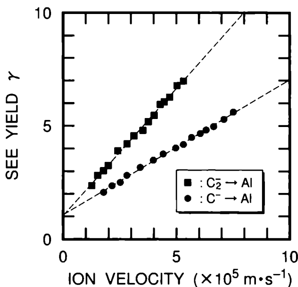

Figure 2.6 Yield of secondary electrons for monatomic and diatomic ions as a function of ion velocity in negative-carbon-ion irradiation onto aluminum. Each broken line denotes the results obtained from the least squares method.

ions penetrate into the target separately. Then,

$$\gamma_{C_2^-} = Kp + Kp + \gamma_0 = K \cdot 2p + \gamma_0. \tag{2.9}$$

The most right side of eq. (2.9) represents that the plot of the yield for monatomic- and diatomic-ion bombardments as a function of ion momentum is on one line, where $2p$ refers to the ion momentum of the diatomic ions at the same velocity as that of the monatomic ions. The ion-momentum plot of Fig. 2.6 is shown in Fig. 2.7. This indicates the good consistency with eq. (2.9) and the efficient plot illustrating kinetic emission. Thus, the additivity property of the yield holds in negative-ion bombardment as well as positive-ion bombardment. In addition, eq. (2.9) suggests that secondary electron emission induced by negative ions comprises kinetic emission and another emission which always causes one electron to be emitted for one negative-ion bombardment.

Next, a comparison of the yield between carbon ions (closed circles) and oxygen ions (open circles), i.e., a comparison of bombardments using different ion elements, is made. Figure 2.8 shows that the yield for negative oxygen ions increases in proportion to ion velocity in the same way as negative carbon ions, and is slight larger than that for negative carbon ions. The feature was also observed for the other conductive materials. It is seen from eqs. (2.3) and (2.4) that the yield becomes large as the projectile atomic number is larger, even if the relationship, $\Lambda \propto Z_1^{-0.2}$[82], is taken into account. This is consistent with the experimental result shown in Fig. 2.8.

2.3.3.3 Ion current density dependence

Figure 2.9 shows the dependence of the yield on the ion current density in negative-carbon-ion irradiation onto platinum (closed circles), silicon (closed triangles), and aluminum (closed squares), when the acceleration voltage was 10 kV. The yield for any target material is constant over the measured ion-current-density range below 3 μA·cm^{-2}, indicating that the yield is independent of the ion current density. The ion current density of 3 μA·cm^{-2} corresponds to an ion impinging on an area 2.3 nm square per second. This suggests that each collisional event inside the material is independent within such

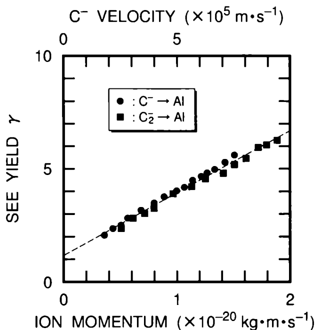

Figure 2.7 Ion-momentum plot of Fig. 2.6. The upper horizontal axis designates the ion velocity of monatomic carbon ions, which is twice the velocity of diatomic carbon ions. The broken line denotes the results obtained from the least squares method.

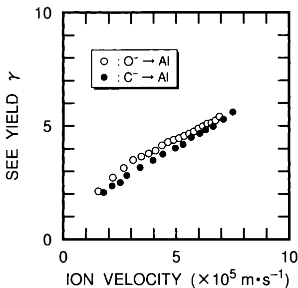

Figure 2.8 Comparison of the yield between the carbon and oxygen ions in negative-ion impact on aluminum as a function of ion velocity.

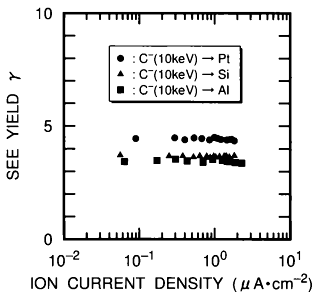

Figure 2.9 Dependence of the yield on the ion current density in negative-carbon-ion irradiation onto platinum, silicon, and aluminum.

an impact frequency.

2.3.4 Results for insulating materials

A study on the secondary electron emission from the insulating surface due to ion bombardment is accompanied by considerably experimental difficulties. For example, the yield of secondary electrons apparently achieves unity in the charge equilibrium. This is because the secondary-electron current changes owing to surface charging so that it becomes equal to the incident-ion current. Therefore, the accurate (or true) yield measurement for the insulating materials requires minimizing surface-charge buildup by supplying the opposite-polarity charges of the accumulated charges.

The yield of insulating materials in positive-ion bombardment has been, so far, reported by some researchers: Batanov[89] measured the yield of alkali halide single crystals, such as sodium chloride and potassium chloride, in lithium- and potassium-ion bombardment. A cleaved slice of the single crystal was heated and bombarded by short single pulses. The value of the yield was 2-9 for 1-6 keV lithium-ion impact on sodium chloride, 2-7 for 1-3 keV potassium ion impact on potassium chloride; the yield measurement for aluminum oxide films by a short pulse counting system with an electron multiplier was carried out by Dietz[90]. The pulse was a 1.8 ns risetime and 4.8 ns width. The yield for 20 keV bombardment by the alkali ions, such as lithium, sodium, cesium, and rubidium ions, was 7-9; Stein and White[91] used quite low ion current of less than 10^{-17} A and a sensitive electron detector (solid state detector) to reduce charge buildup by 4-5 orders of magnitude. The yield was measured for barium, strontium, cesium, and lithium ions incident on aluminum-oxide and titanium-oxide films, and hence the value was 3-6 for 10-40 keV strontium-ion impact on aluminum oxide, 4-7 for 15-40 keV cesium-ion impact on titanium oxide, for example.

This study presents the yield measurement during irradiation onto the insulating material by a simple method using a thin oxide film and low ion current at room temperature. The manner is basically applicable irrespective of the ion polarity. The yield measurement for the insulating materials was carried out using the apparatus shown in Fig. 2.4,

when the limiter of a diameter of 5 mm was attached to be aligned with the limiter of the apparatus in order to reduce the incident-ion current. The thin oxide film of less than a few hundred nm is expected to have a lower resistance and a higher leak current flow than the thick insulating substrate. If the charge-compensation current neutralizes the surface charges and suppress the charge buildup, the true yield for the insulating material will be obtained.

Thermally grown silicon dioxide (SiO_2) films 120 nm and 360 nm thick on silicon substrates were prepared as the insulator film. During the yield measurement the vacuum in the implantation chamber was 1×10^{-3} Pa or lower, and dose was less than 1×10^{16} ions·cm^{-2}.

Figure 2.10 shows the apparent yield in negative-carbon-ion irradiation, calculated from the measured data, I_{se} and I_{cc}, according to eq. (2.7). The apparent yield becomes unity in the higher ion-current-density region, except for 20 keV negative-carbon-ion impact on the 120 nm SiO_2 film. The apparent yield of one indicates that the insulating surface is charged. However, the apparent yield approaches to a certain value, not one, with decreasing ion current density. This suggests that the charge-compensation current compensates the accumulated charges to reduce the surface charging. This phenomenon is considered as follows. Positive charges generated as a result of electron excitation have an effect on secondary electron emission under insufficient charge compensation; in contrast, there exist no positive charges to influence under sufficient compensation. Therefore, the apparent yield was regarded as the true yield, below 1 nA·cm^{-2} for the 120 nm SiO_2 film; 0.3 nA·cm^{-2} for 360 nm. The yields at any ion energy agreed with each other within a relative error of 10 % irrespective of the different SiO_2 film thickness. This demonstrates that the measurement method is valid.

Only in negative-carbon-ion impact on the 120 nm SiO_2 film at an ion energy of 20 keV, the apparent yield remains almost constant with respect to the ion current density. This is explained from the relationship between the projected range and the insulator film thickness. The TRIM[92] calculation indicates that some of carbon ions incident on SiO_2 at an ion energy of 20 keV can reach up to a depth of 120 nm from the surface.

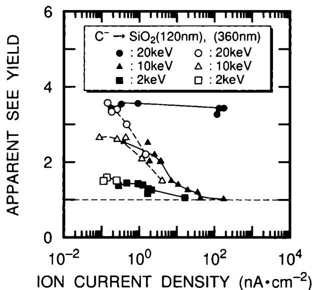

Figure 2.10 Apparent yield of secondary electrons emitted from the SiO_2 films as a function of ion current density during negative-carbon-ion irradiation.

Thus, the charge-compensation current was easy to flow from, or, to the silicon substrate, because the projectiles are penetrating while generating the liberated electrons to apparently reduce the insulator-film thickness. However, the increase in the charge-compensation current resulting from the apparent reduction of the film thickness has no effect on secondary electron emission. This is because the liberated electrons generated around the interface between the insulating layer and the silicon substrate cannot reach the surface and escape into a vacuum, on account of the escape depth of approximately 10 nm for the insulating materials[68].

Figure 2.11 shows the dependence of the yield on the ion momentum, when the SiO_2 films were bombarded by negative-monatomic- (closed circles) and diatomic-carbon (closed squares) ions. The broken line designates the results obtained by the least squares method and all plots for negative carbon ions are approximately on the line except for a few of the lowest ion-momentum plots. The yield in proportion to the ion momentum indicates that the main mechanism of secondary electron emission from the insulating material due to negative-ion bombardment is kinetic emission. It is also observed that an intersection of the line with the vertical axis is approximately one. These features are the same as for the conductive materials shown in § 2.3.3.

A comparison of the yield between the carbon (closed circles) and oxygen (open circles) ions is made. Figure 2.12 shows the yield in negative-carbon- and oxygen-ion bombardment as a function of ion velocity. It is seen that, except for the yield of one corresponding to the intercept, the yield for negative-oxygen-ion bombardment is larger by approximately 8 % than that for negative-carbon-ion bombardment. From eqs.(2.3) and (2.4), the yield for oxygen-ion impact on silicon dioxide is larger by approximately 15 % than that for carbon-ion impact on silicon dioxide at the same ion velocity, on the basis of Bragg's rule[93]. This almost explains the tendency shown in Fig. 2.12. This is the same property as the case of the conductive materials, indicating that secondary electron emission in negative-ion bombardment does not depend on the conductivity of target materials but basically originates from the same mechanism.

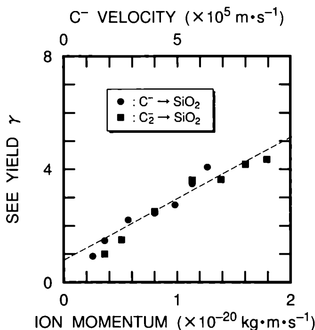

Figure 2.11 Yield of secondary electrons emitted from the SiO_2 film as a function of ion momentum in negative-carbon-ion bombardment. The upper horizontal axis designates the ion velocity of monatomic carbon ions, which is twice the velocity of diatomic carbon ions. The broken line is obtained using the least squares method.

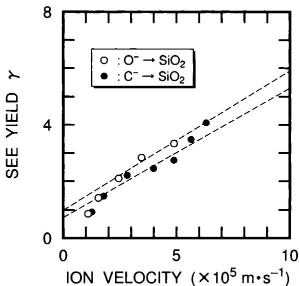

Figure 2.12 Comparison of the yield between the carbon and oxygen ions in negative-ion irradiation onto the SiO_2 film as a function of ion velocity.

2.3.5 Comparison with positive-ion-induced secondary electrons

The yields in positive- and negative-carbon-ion irradiation onto platinum and silicon dioxide as a function of ion velocity are shown in Fig. 2.13. The open and closed symbols designate the yield for positive and negative carbon ions, respectively. In addition, the broken lines designate the results obtained by the least squares method, taking into account the data of diatomic-carbon-ion bombardment for the silicon-dioxide plots. Figure 2.13 indicates that the lines are almost parallel to each other for each target, and that the yield for negative carbon ions is larger by approximately one unit than that for positive carbon ions over the measured ion velocity range. This is true for both materials irrespective of the conductivity. The same feature as that shown in Fig. 2.13 was also observed for the other targets such as gold.

The yield difference, deriving from the polarity of the ions incident on the same target, can be considered to originate from an electron bound with a negative ion. A negative ion, in general, holds an extra electron with binding energy of electron affinity, which is as low as approximately a few eV and, for example, the magnitude of monatomic carbon is 1.268 eV[94]. Thus, it is likely that negative ions easily release the extra electron in impact on the surface. It is considered, therefore, that secondary electrons induced by negative ions originate from kinetic emission due to excitation of valence electrons by the impinging ions and electron detachment from the negative ions in ion bombardment.

2.4 Energy distribution measurement

2.4.1 Measurement apparatus and method

Figure 2.14 shows a hemispherical beam collector of 210 mm diameter used to measure the energy distribution of secondary electrons in addition to the incident-ion current. The ion beam is incident perpendicular to the surface of the specimen mounted at the center of the collector. During the energy distribution measurement, the extraction voltage of +10 V was applied to the collector, while the specimen was at ground potential to prevent

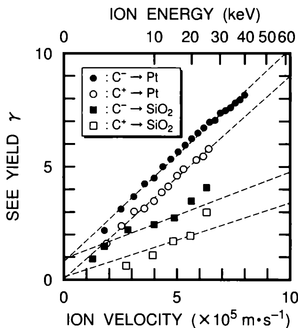

Figure 2.13 Yields of secondary electrons in positive- and negative-carbon-ion impact on platinum and SiO_2 as a function of ion velocity. The broken lines designate the results obtained by the least squares method.

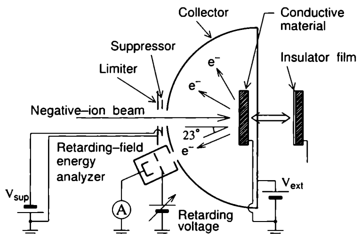

Figure 2.14 Schematic diagram of the measurement apparatus for the energy distribution of secondary electrons. A retarding-field energy analyzer with an electron multiplier is installed.

the space charge formed by the emitted secondary electrons from affecting the low-energy secondary-electron trajectory. That is, the collector plays a role of a secondary-electron extractor in measuring the energy distribution. The hemispherical collector, furthermore, helps the electrical field line to point toward the radius direction. In measuring the incident-ion current, the collector was connected directly with an amperemeter.

A limiter of 8 mm diameter attached at the entrance of the apparatus was grounded. A suppressor, located between the limiter and the collector, was biased at −50 V. The conductance of this apparatus is so small that the gas pressure inside the collector may be higher than that outside the collector. Hence, the meshes of 20 wires each 10 mm long and of diameter 0.15 mm (49 % of the optical transparency), made of stainless-steel wire, were attached to 54 % of the rear plate of the apparatus to improve the conductance and to decrease the pressure inside the collector.

The secondary-electron trajectory can be easily affected by the magnetic field. Therefore, Helmholtz coils of 700 mm cube was set around the implantation chamber so that the magnetic fields of the earth, rotary pumps, and an analyzing magnet can be canceled out. As a result, the magnetic field of a 100 mm cube magnetic-field space at the center of the implantation chamber, where the apparatus shown in Fig. 2.14 was set, was reduced to less than $5 \mu T$. In general, the magnitude of the terrestrial magnetism is approximately 30 μT. Therefore, the secondary electrons with an energy larger than 0.3 eV can be analyzed in theory.

The energy of charged particles such as electron can be analyzed by using the following various effects: a retarding field (retarding-field type), a deflection field (electrostatic-prism type, cylindrical-mirror type), an aberration of a lens (Einzel-lens type, solenoid-lens type), the difference of velocities (time-of-flight type), etc. This study chose a retarding-field type energy analyzer which has the advantages of a high signal-to-noise ratio, a wide energy-analyzable range, a quick response, and easy fabrication. The energy analyzer was installed in the apparatus so as to minimize an angle which the secondary-electron beam entering the analyzer makes with the incident-ion beam. As a result, the angle was set at 23 °, as shown in Fig. 2.14. Accordingly, this study does not take into account the

angular dependence of the secondary-electron energy distribution.

In the energy distribution measurement during negative-ion irradiation onto the insulating material as well as the yield measurement, a thin insulator film on a silicon substrate was mounted instead of the conductive material, as shown in Fig. 2.14.

Figure 2.15 illustrates the retarding-field energy analyzer in detail. The energy analyzer consists of six electrodes of a limiter, an accelerator, a retarding electrode, a reaccelerator, a suppressor, and a detector of an electron multiplier. The meshes made of gold-evaporated tungsten wire are attached to the accelerator, the retarding electrode, and the reaccelerator in order to form the uniform electric field. The optical transparency for each mesh is about 78 % (100 wires each 25.4 mm long and of diameter 0.03 mm). A collimator of 4.5 mm diameter and 15 mm long, removing the electrons with large transverse energy, was attached at the entrance of the energy analyzer to improve the energy resolution. Thereby, the incident angle of secondary electrons, θ_{se}, was reduced to less than 1.3 °. To improve the energy resolution further, an aspect ratio, d_{acc}/l_{ret}, which is the ratio of the aperture diameter of the accelerator, d_{acc}, to the length of the retarding region between the accelerator and the retarding electrode, l_{ret}, was designed as small as 0.37. The energy resolution in theory, $\Delta E/E$, is given by[94]

$$\frac{\Delta E}{E} = \frac{1}{2}\left(\theta_{se} + \frac{d_{acc}}{8l_{ret}}\right)^2, \tag{2.10}$$

indicating that the energy resolution is more improved as the aspect ratio is reduced. According to eq. (2.10), this energy analyzer will have the high energy resolution of 2.4×10^{-3}. The energy distribution measurement of the thermions emitted from an oxide cathode has indicated that the instrumental function of the analyzer is Gaussian-like and the full width at half-maximum is 0.54 eV. The energy resolution calculated by regarding the width as ΔE is 6.8×10^{-3}. This is close to the theoretical value of 2.4×10^{-3}. In the energy distribution measurement, the instrumental function of the analyzer has an effect on the shape of the measured energy distribution. That is, the energy distribution obtained by energy analysis is a convolution of the true energy distribution with the instrumental function. The above result describes, however, that the effect of the instrument function is small

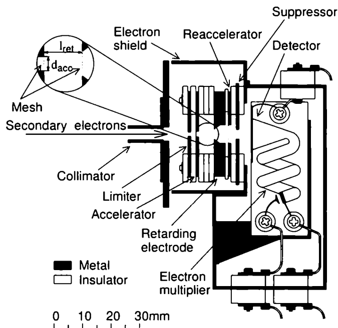

Figure 2.15 Schematic diagram of a retarding-field energy analyzer, which consists of six electrodes of a limiter, an accelerator, a retarding electrode, a reaccelerator, a suppressor, and a detector of an electron multiplier.

compared with the unstability due to the ion source and the electric noise. Hence, no deconvolution was made in this study.

The potential distribution on the center line of the energy analyzer is shown in Fig. 2.16. The electron shield as well as the limiter and the accelerator was biased at +80 V. The suppressor was kept at the higher potential than the limiter, the accelerator, and the reaccelerator in order to prevent the secondary electrons generated at each electrode from entering the detector. The voltage variation from −40 V to +10 V was applied to the retarding electrode for energy analysis. The secondary electrons passing through the retarding-potential barrier and then entering the electron multiplier were accelerated at high voltage of 2.0–2.5 kV, and hence the secondary-electron current was amplified to 10^6–10^7. As a result, the electron multiplier improves the sensitivity.

A block diagram of the energy-analyzing system is shown in Fig. 2.17. The secondary-electron current amplified by the electron multiplier is converted into the voltage signal of 10 mV maximum at an electron multiplier P. S. An isolation amplifier separates the signal from the output of the electron multiplier P. S. including the acceleration voltage of 2.0–2.5 keV, and then amplifies only the signal by a factor of 100. The retarding voltage was swept from −40 V to +10 V by a retarding voltage P. S. which amplifies the original voltage generated by a voltage sweeper. The retarding voltage and the signal output were led to an XY recorder.

Since the energy analyzer is retarding-field type, the signal current, $I_{sc}(V_{ret})$, detected by sweeping the retarding voltage, V_{ret}, is integral of the energy distribution, $N(E)$:

$$I_{sc}(V_{ret}) = I_{sc}^{*} \int_{-eV_{ret}}^{E_{max}} N(E)\mathrm{d}E, \tag{2.11}$$

where E_{max} is the maximum energy of secondary electrons and the definite integral from 0 eV to E_{max} of the energy distribution is normalized to one. The absolute value of I_{sc}^{*} is the maximum in the detected current and hence from eq. (2.11),

$$I_{sc}^{*} = I_{sc}(0). \tag{2.12}$$

The energy distribution is given by differentiation of the signal current with respect to

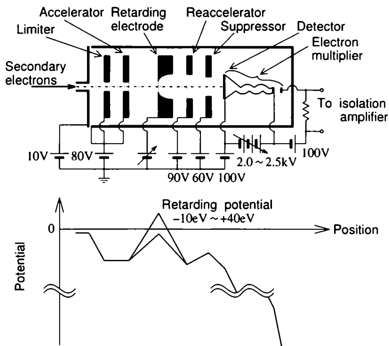

Figure 2.16 Potential distribution on the center line of the energy analyzer. The energy analysis of secondary electrons was done by the retarding potential of −10 eV to +40 eV.

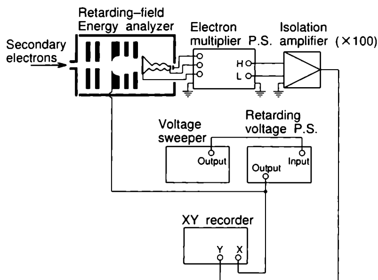

Figure 2.17 Block diagram of the arrangement for measuring the energy distribution of secondary electrons.

retarding voltage:

$$N(-eV_{ret}) = -\frac{1}{I_{se}^{*}}\frac{dI_{se}}{dV_{ret}} \propto \frac{dI_{se}}{dV_{ret}}. \qquad (2.13)$$

Figure 2.18 shows a set of typical examples of the detected signal current and the energy distribution obtained according to eq. (2.13) as a function of retarding voltage. A differentiation was numerically done before smoothing.

2.4.2 Results for conductive materials

The energy distribution measurement during negative-ion irradiation onto the conductive materials was carried out. The results, the dependence of the energy distribution on ion energy and ion current density, will be described below.

Figure 2.19 shows the energy distributions of secondary electrons emitted from the aluminum surface onto which negative carbon ions were irradiated at ion energies of (a) 10 keV, (b) 20 keV, and (c) 30 keV with ion current density of less than 300 nA·cm^{-2}. In Fig. 2.19, E denotes the electron energy measured from the vacuum level at the retarding electrode and have the following relation to the retarding voltage: $E = -eV_{ret}$. That is, the abscissa in Fig. 2.19 is reverse to that in Fig. 2.18. It is observed from Fig. 2.19 that every distribution has a peak at about 1 eV and a long tail extending toward the high-energy region. It is known, in general, that the energy distribution of secondary electrons by positive-ion bombardment[72,73] or electron bombardment[67,69,95,96] has a peak at 1-2 eV and a long tail extending toward the high-energy region. Figure 2.20 shows the energy distribution of secondary electrons emitted from the aluminum surface in 20 keV negative-carbon-ion bombardment by the solid curve together with that in 20 keV positive-carbon-ion bombardment by the broken curve. The latter was measured in the same implanter as the former, only by substituting positive-ion source for negative-ion source. The shape of the energy distribution in negative-ion bombardment is close to that in positive-ion bombardment. Unfortunately, this study did not reach the quantitative comparison of the energy distribution between the different ion polarities.

As shown in Fig. 2.19, the shape appears to be almost independent of the ion energy. Figure 2.21 shows the dependence of the full width at half-maximum (FWHM) on ion

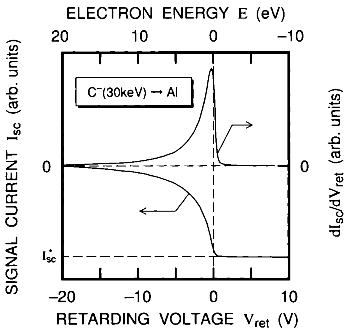

Figure 2.18 Typical examples of the detected signal current and the energy distribution as a function of retarding voltage.

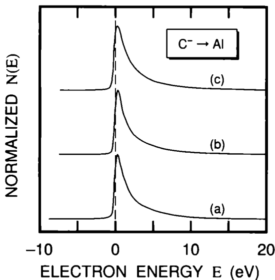

Figure 2.19 Normalized energy distributions of secondary electrons when negative carbon ions at (a) 10 keV, (b) 20 keV, and (c) 30 keV are irradiated onto the aluminum surface. The horizontal axis is taken as the electron energy measured from the vacuum level at the retarding electrode.

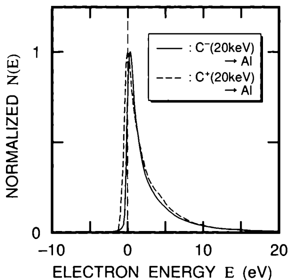

Figure 2.20 Normalized energy distributions of secondary electrons in positive- and negative-carbon-ion impact on the aluminum surface at an ion energy of 20 keV.

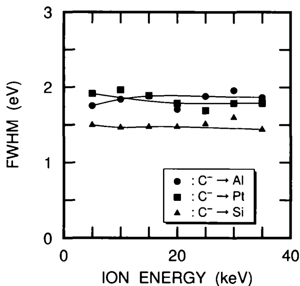

Figure 2.21 FWHM of the energy distribution as a function of ion energy in negative-carbon-ion irradiation onto the conductive materials.

energy in negative-carbon-ion irradiation onto aluminum (closed circles), platinum (closed squares), and n-type silicon (closed triangles). This indicates that the shape of the energy distribution depends on the material rather than the ion energy. Since the ions penetrate more deeply into the target material with increasing ion energy, the majority of electrons become excited in the deeper region of the material. Irrespective of the ion energy, the origin of secondary electrons is the top layer of 0.5–2 nm from the surface[68]. Therefore, the shape of the energy distribution is independent of the ion energy.

Figure 2.22 shows the FWHM and the most probable energy as a function of ion current density below 1.5 μA·cm^{-2}, in negative-carbon-ion impact on platinum at an ion energy of 10 keV. The solid symbols designate the FWHM and the most probable energy for monatomic-ion bombardment; the open symbols designate those for diatomic-ion bombardment to the contrary. Both of the FWHM and the most probable energy remain steady in the ion current density region below 1.5 μA·cm^{-2}, and the values for monatomic- and diatomic-ion bombardment are almost equal to each other. The same feature was observed in the other negative-carbon-ion-induced conductive materials, such as aluminum and silicon.

2.4.3 Results for insulating materials

The energy distribution measurement for negative-ion-induced insulating materials as well as the yield measurement was carried out by using a thin oxide film and low ion current to reduce surface charging.

Figure 2.23 shows the energy distributions of secondary electrons emitted from the 120 nm SiO_2 film during negative-carbon-ion irradiation at ion energies of (a) 10 keV, (b) 20 keV, and (c) 30 keV with ion current density of approximately 2 nA·cm^{-2}. The energy shift in the energy distribution was observed: the energy distribution appears in more negative energy region as the ion energy is lower. The energy shift is more evident in Fig. 2.24, showing the FWHM (closed circles) and the most probable energy (closed squares) of the energy distribution as a function of ion energy. The most probable energy decreases with decreasing ion energy and becomes steady below 15 keV. This indicates

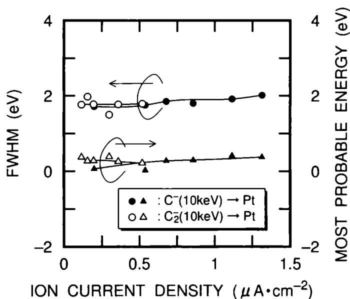

Figure 2.22 FWHM and most probable energy of the energy distribution as a function of ion current density in negative-carbon-ion irradiation onto platinum.

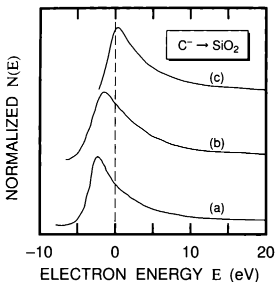

Figure 2.23 Normalized energy distributions of secondary electrons when negative carbon ions at ion energies of (a) 10 keV, (b) 20 keV, and (c) 30 keV with approximately 2 $nA \cdot cm^{-2}$ were irradiated onto the SiO_2 film of 120 nm thick. The horizontal axis is taken as the electron energy measured from the vacuum level at the retarding electrode.

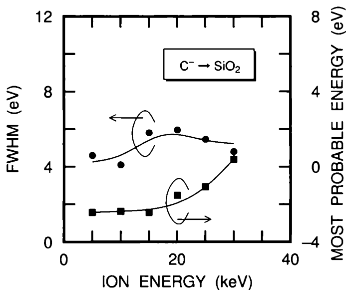

Figure 2.24 FWHM and most probable energy of the energy distribution as a function of ion energy in negative-carbon-ion impact on the SiO_2 film of 120 nm thick at an ion current of almost 2 $nA{\cdot}cm^{-2}$.

that the target surface is positively charged in comparison with the ground potential because the charge compensation is insufficient owing to a low ion energy. The positive charging of the insulating material during negative-ion irradiation is not consistent with a discussion in Chapter 4. This is because this positive charging results from the charge-compensation current flowing from the film surface to the rear resulting from the yield of more than one. Therefore, this case is essentially different from the negative charging of the insulating materials due to no charge-compensation current described in Chapter 4.

The resistance of the SiO_2 film can be reduced because the projected range is extended with an increase in ion energy. As a result, the surface approaches to the ground potential. Therefore, it is considered that the energy distribution for 30 keV ion bombardment is likely to be close to the true distribution. However, Fig. 2.10 shows that there occurs the charging reduction at an ion energy of 20 keV. It is considered that the difference is not due to essential property but results from the difference of the samples, the slight measurement conditions, etc.

Besides, Fig. 2.24 shows that the FWHM remains almost steady with respect to ion energy although the values of the FWHM are somewhat scattered.

2.5 Discussion

Secondary electron emission induced by positive ions is divided into potential emission and kinetic emission. From the measured data of the yield and the energy distribution, it was clarified that secondary electron emission induced by negative ions as well as that by positive ions is mainly kinetic emission. It is obvious that no potential emission occurs in negative-ion impact because negative ions have no ionization potential. On the other hand, negative-ion impact can cause an electron detachment from a negative ion. The presence of the detached electron of the emitted secondary electrons was explicitly observed in the measured data of the yield. That is, the yield for negative ions is larger than that for positive ions and the difference is one. This suggests that detached electrons neither interact with nor excite conduction and/or valence electrons in the target. Since

potential emission is caused by a process of Auger neutralization and de-excitation, the yield of the escaping electrons is 0.1 or lower[76]. This value is quite far from one. The low yield originates from only a small escape probability of the excited electrons in the target. Therefore, it is concluded that no Auger process due to the detached electrons, such as potential emission, occurs in negative-ion bombardment. Now, let us consider the electron detachment by introducing electron detachment cross sections. Assume that the initial amount of negative ions, N_0^-, is reduced to N^- while negative ions are penetrating the material whose density is n by the path length, L_p. Then the following equation holds:

$$N^- = N_0^- \exp(-n\sigma_{-10}L_p), \tag{2.14}$$

where σ_{-10} is single-electron detachment cross section (neutralization). The single-electron detachment cross section for negative carbon ions passing through the gas, such as argon, nitrogen, and xenon, was measured[97,98]. The value is of the order of 10^{-15} cm^2 and independent of the ion velocity for 3–9×10^5 m·s^{-1}. It is assumed that the data is applicable for the materials used in this study. Since the density of the materials such as aluminum, platinum, gold, and silicon used in the measurement is 5.0–6.6×10^{22} atoms·cm^{-3}, put $n = 6\times10^{22}$ atoms·cm^{-3}. Furthermore, suppose $\sigma_{-10} = 1\times10^{-15}$ cm^2 and L_p=0.2 nm, corresponding to one atomic layer. Then, the result calculated from eq. (2.14) indicates that 30 % of electrons are released from negative ions at one-atomic-layer depth from the surface. In fact, the electrons of the target material ought to have an effect on the detachment. Therefore, it is considered that electrons detached from negative ions were detected in the measurement.

The dose was on the order of 1×10^{16} ions·cm^{-2} in the measurement of secondary electrons, because this study assumes ion implantation in semiconductor fabrication. A dose of 1×10^{16} ions·cm^{-2} can easily change the surface conditions of the target owing to the dose, amorphousization, etc. In the energy distribution measurement, the most probable energy of the measured energy distribution includes the contact potential difference: when the work function of the specimen is larger than that of the retarding electrode, the energy

Table 2.1 Work function[99] before implantation and the difference of the work function after negative-carbon-ion implantation of 10^{16} ions·cm^{-2} dose from that before implantation. Data of the work function for carbon is shown as a reference.

Material	Work function (eV)	Difference (eV)
Platinum	5.29	−0.1
Carbon	4.39	
Aluminum	3.74	+0.9

distribution shifted by the contact potential difference toward the high-energy region will be observed; in the opposite case, the energy shift toward the negative-energy region will be observed. However, the most probable energy of the energy distribution induced by negative ions is approximately 0–1 eV, which was almost the same value irrespective of the target materials. Thus, the difference of the most probable energy among the target materials due to the energy shift was not explicitly observed. Table 2.1 shows the difference of the work functions before and after negative-carbon-ion implantation of 10^{16} ions·cm^{-2} dose, obtained by Kelvin method[100]. The difference in Table 2.1 corresponds to the work function after implantation minus that before implantation. As a result of carbon-ion implantation, the work function of platinum larger than that of carbon was decreased by 0.1 eV, while the work function of aluminum smaller than that of carbon was increased by 0.9 eV. This indicates that the work function of the carbon-implanted material approaches to the work function of carbon. In a dose of 10^{15} ions·cm^{-2} or lower, in contrast, the energy shift was observed. Hence, it is considered that almost the same most probable energy irrespective of the different target materials is due to the dose of 10^{16} ions·cm^{-2}. This dose corresponds to the small percentage of occupation by the impurity.

2.6 Summary

The significant parameters of negative-ion-induced secondary electrons, the yield and the energy distribution, were studied to clarify the charging mechanism in negative-ion implantation. Hence, all measurements were carried out under the ion-implantation conditions in semiconductor fabrication, i.e., the residual gas pressure of 10^{-4} Pa order and a dose of 10^{16} ions·cm^{-2}.

The results for the yield measurement have revealed the yield proportionality to ion velocity in the region of 10^5 to 10^6 m·s^{-1}. This has indicated that the secondary electron emission induced by negative ions as well as that by positive ions is mainly the kinetic mechanism. In addition, it has been discovered that the magnitude of the yield in negative-ion bombardment is larger by one unit than that in positive-ion bombardment. This is concluded to be due to the detachment of the extra electron bound to the negative ion owing to ion impact on a solid surface. Therefore, the negative-ion-induced secondary electrons consists of this extra electron and the electrons originating from kinetic emission. On the other hand, it was observed that the energy distribution of secondary electrons induced by negative ions has a peak at about 1 eV and a long tail extending toward the high-energy region. This has demonstrated that the shape of the energy distribution induced by negative ions is close to that induced by electrons and positive ions. No other peak, such as an Auger peak, was observed in the energy distribution. In addition, these parameters are independent of ion energy (velocity) and ion current density in the ion energy range below 40 keV with an ion current density of less than a few mA·cm^{-2}, while they depend somewhat on target materials.

Most measurements were carried out by using negative carbon ions. However, some results for negative oxygen ions has showed the same properties as that for negative carbon ions. This demonstrates that the properties described above are not restricted only to negative carbon ions, because the secondary-electron emission phenomenon originates mainly from kinetic interactions.

Chapter 3

The Charging Mechanism of Isolated Electrodes in Negative-ion implantation

3.1 Introduction

In the recent trend of decreasing the gate oxide thickness in semiconductor fabrication, the charging problem which brought by ion implantation has become even more serious. The charging voltage in excess of 10 V during the fabrication process will damage a 10 nm oxide film permanently and catastrophically, because a high quality oxide film typically has a dielectric breakdown strength of 10 $MV \cdot cm^{-1}$. The traditional solution to the positive charging of wafers induced by positive ions has been the use of electron floodguns which shower on the wafer surface during implantation. However, such an external charge neutralization system always has the possibility of negative charging due to high-energy electrons.

Negative-ion implantation, on the contrary, introduces negative charges into the wafer, and will be able to keep the charging voltage of the insulating and the insulated materials close to the ground potential. In fact, the preliminary experiment has indicated the low charging during negative-ion implantation, as shown in Figs. 1.2 and 1.3. Thus, negative-ion implantation is intrinsically less prone to charging unlike positive-ion implantation. Accordingly, it is expected that negative-ion implantation will be effective as charging-free implantation.

This chapter describes the charging properties of an electrically insulated material,

which is designated an isolated electrode, during negative-ion implantation[35,49,53-56]. The charging voltage of isolated electrodes was measured by varying ion energy (velocity), ion current density, ion species and target material, and compared with that in positive-ion implantation to clarify the low charging of isolated electrodes in negative-ion implantation. A charging model based on the emitted secondary electrons is proposed to explain the positive, low charging voltage in the equilibrium charging. Furthermore, the dependence of the charging voltage on the yield is also discussed, taking into account the dependence of the yield on the ion velocity.

3.2 Charging voltage measurement

3.2.1 Measurement apparatus

Figure 3.1 shows the measurement apparatus for the charging voltage of an isolated electrode during negative-ion implantation. An isolated electrode was mounted at the center of the hemispherical shield of 210 mm diameter. The isolated electrode typically consists of a 30 mm × 30 mm square sheet made of a conductive material sheet or film on an alkali-free glass plate 1.1 mm thick. A mass-separated negative-ion beam enters the apparatus through a limiter and a suppressor, and then strikes the electrode surface. The limiter 8 mm in diameter was at ground potential, while the suppressor was biased by −50 V to prevent the secondary electrons generated at the limiter and the isolated electrode from going in and out, respectively. Thereby, it is possible to precisely examine the charging of the isolated electrode and the relationship of the charging with secondary electrons.

The charging voltage of an isolated electrode during negative-ion implantation was measured by using a noncontacting electrostatic voltmeter outside the vacuum. It is possible for the voltmeter to measure the voltage more than the order of kV, but the resolution is as large as 10 V. Thus, a high-input-impedance (1000 GΩ) voltmeter was substituted in measuring the charging voltage less than a few tens volts.

The following conductive materials were prepared for an isolated electrode: aluminum, platinum, gold, and n-type silicon. All measurements were carried out under gas

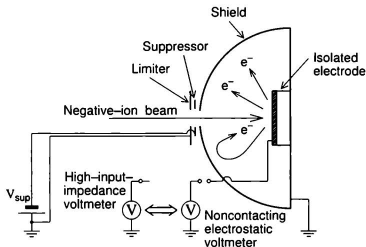

Figure 3.1 Schematic diagram of the measurement apparatus for the charging voltage. The charging voltage of an isolated electrode is measured by a noncontacting electrostatic voltmeter or a high-input-impedance voltmeter.

pressures of the order of 10^{-4} Pa and dose was $1\text{-}5\times10^{16}$ ions·cm^{-2}.

3.2.2 Results of measurement

The charging voltage measurement of isolated electrodes during negative-ion implantation was carried out varying the implantation conditions: ion energy (velocity), ion species, and ion current density. The dependence of the charging voltage on each parameter will be discussed in the succeeding sections.

3.2.2.1 Ion energy (velocity) dependence

Figure 3.2 shows the charging voltage of the isolated electrodes, such as Pt/glass (closed circles), Al/glass (open squares), and Si/glass (closed triangles), during negative-carbon-ion implantation. The ion current density was below a few hundreds nA·cm^{-2} as follows: 4.4–100 nA·cm^{-2} for $C^- \rightarrow$ Pt/glass, 2.8–420 nA·cm^{-2} for $C^- \rightarrow$ Al/glass, 2.4–76 nA·cm^{-2} for $C^- \rightarrow$ Si/glass. Although the ion current density depends on the ion energy, the charging voltage of the isolated electrodes remains steady on the order of ion current density below a few μA·cm^{-2}, as described later. Thus, Fig. 3.2 reflects the property due to the ion energy.

The isolated electrode during negative-ion implantation is positively charged and any curve increases slowly with an increase in ion energy, as shown in Fig. 3.2. Even at an ion energy of 40 keV, the charging voltage is still as low as several volts irrespective of the target materials. A slight difference of the charging voltage by a few volts among the target materials indicates the charging voltage of the negative-ion-implanted isolated electrodes has a slight dependence on the target material.

Figure 3.3 is the plot of the charging voltage against ion velocity, in which the same data as Fig. 3.2 was used. It is seen that the charging voltage is almost proportional to ion velocity. This implied that the property is close to that of the yield of secondary electrons. The relationship between the charging voltage and the yield will be discussed later.

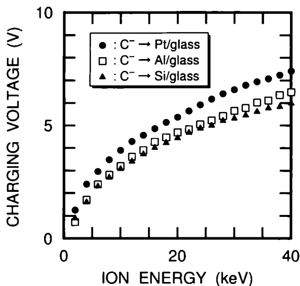

Figure 3.2 Charging voltage of the isolated electrodes as a function of ion energy, when negative carbon ions were implanted into Pt/glass, Al/glass, and Si/glass.

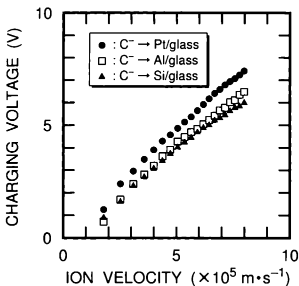

Figure 3.3 Charging voltage of isolated electrodes as a function of ion velocity during negative-carbon-ion implantation. The data is the same as Fig. 3.2.

3.2.2.2 Ion species dependence

The ion-energy dependence of the charging voltage is shown in Fig. 3.4, when negative carbon ions were implanted into an isolated electrode (Al/glass). The closed circles and squares designate the charging voltage for monatomic and diatomic ions, respectively. The charging voltage in negative-dicarbon-ion bombardment is larger by about 1 V than that in negative-carbon-ion bombardment at the same ion energy of 20 keV to 40 keV, and the voltage difference decreases with decreasing ion energy. The similar tendency was also observed for the other conductive materials.

3.2.2.3 Ion current density dependence

The voltage measurement described above was carried out below the ion current density of a few hundreds nA$\cdot$cm^{-2}. The charging voltage of isolated electrodes, such as Pt/glass (closed circles), Al/glass (open squares), and Si/glass (closed triangles), during negative-carbon-ion implantation remains almost constant in the ion current density range of less than 2 μA$\cdot$cm^{-2}, as shown in Fig. 3.5. However, it is seen that the charging voltage gradually decreases with an increase in ion current density.

Figure 3.6 shows the charging voltage as a function of ion current density above 0.1 μA$\cdot$cm^{-2}. The closed circles designate the charging voltage of an isolated electrode (Si/glass) during negative-carbon-ion implantation at 15 keV; the closed squares, during negative-silicon-ion implantation at the same ion energy. The charging voltage remains almost constant up to a few μA$\cdot$cm^{-2}, almost close to 10 μA$\cdot$cm^{-2}. Beyond an ion current density of 10 μA$\cdot$cm^{-2}, however, the charging voltage begins to decrease and becomes 0 V at about 20 μA$\cdot$cm^{-2}. Eventually, the charging voltage reaches -3 V at 50 μA$\cdot$cm^{-2}.

The magnitude of beam potential at the beam center formed by an incident negative-ion beam is shown together in Fig. 3.6 by the solid curve. The beam potential is based on the assumption of a cylindrical beam transported through a cylindrical shield. Then, the beam potential, ϕ_{bp}, at the beam center is estimated as follows:

$$\phi_{bp} = -0.039 J_{ion} \sqrt{M}, \tag{3.1}$$

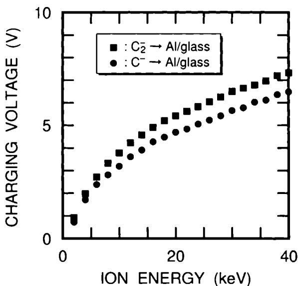

Figure 3.4 Comparison of the charging voltages of an isolated electrode (Al/glass) between monatomic and diatomic ions in negative-carbon-ion implantation as a function of ion energy.

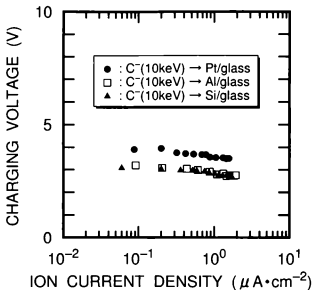

Figure 3.5 Charging voltage of isolated electrodes as a function of ion current density below 1 μA·cm^{-2}, in negative-carbon-ion implantation into Pt/glass, Al/glass, and Si/glass.

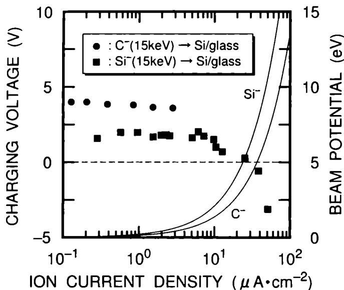

Figure 3.6 Charging voltage of isolated electrodes as a function of more than 0.1 μA·cm^{-2} ion current density in negative-carbon- and silicon-ion implantation. The solid curves denote the magnitude of beam potential formed by space charge of an incident negative-ion beam.

where J_{ion} and M are the ion current density (unit in μA·cm^{-2}) and the atomic weight, respectively; the diameter and the energy of the cylindrical beam are 8 mm and 15 keV, respectively; the radius of the cylindrical shield is 100 mm. It is seen from Fig. 3.6 that a drop of the charging voltage coincides with a sharp increase in the beam potential. This is considered to be attributed to the negative beam-potential in front of the electrode pushing the emitted secondary electrons back to the electrode surface. Since a large number of secondary electrons has low energy less than a few eV, as described in § 2.4, the beam potential at several eV can easily be a potential barrier in front of the electrode surface.

3.2.3 Comparison with positive-ion-implanted isolated electrodes

In this section, a comparison of the charging voltage is made between negative-ion implantation and positive-ion implantation. The charging voltage measurement was carried out under the same conditions and no charge compensation was performed.

Figure 3.7 shows the charging voltage of an isolated electrode (Al/glass) during positive-carbon-ion implantation (open circles) together with that during negative-carbon-ion implantation (closed circles). The broken line in the figure denotes the acceleration voltage corresponding to the ion energy. The charging voltage of the isolated electrode during positive-ion implantation is close to the acceleration voltage. In contrast, the charging voltage during negative-ion implantation is quite low at several volts positive in spite of the same acceleration voltage. It is understood that positive-ion implantation into an isolated electrode is equivalent to the positive-charge accumulation to a capacitor. Furthermore, secondary electron emission from the electrode enhances the rise of the charging at the beginning of implantation: without secondary electron emission, the positive-charge accumulation ratio is given by I_0; with secondary electron emission, the ratio rises to $(1+\gamma)I_0$, where I_0 is positive-ion current and γ is the yield of secondary electrons. After brief implantation, the ratio approaches to I_0 because the emitted secondary electrons, of which energy is almost as low as several eV, are pulled back to the electrode

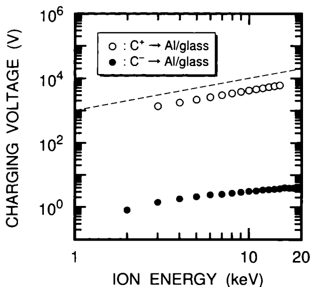

Figure 3.7 Comparison of the charging voltage of an isolated electrode as a function of ion energy between positive- and negative-carbon-ion implantation. The broken line denotes the acceleration voltage corresponding to the ion energy.

owing to its positive potential. Thus, positive-ion implantation inherently requires external charge neutralization by using negative charges such as electrons to suppress the charge buildup.

3.3 Modelling of negative-ion-implanted isolated electrodes

3.3.1 Equilibrium charging-voltage equation

The measured data have revealed the positive, low equilibrium charging of isolated electrodes during negative-ion implantation, except for ion current density of more than 10 μA$\cdot$cm^{-2}. In this section, attention is given to the charging phenomenon of isolated electrodes during negative-ion implantation in the ion-current-density range below 1 μA$\cdot$cm^{-2}. Above an ion current density of 10 μA$\cdot$cm^{-2}, the negative beam-potential should be taken into account. In modelling the charging phenomenon of isolated electrodes during negative-ion implantation, this study concentrated only on the secondary electrons emitted from the electrode surface, because the number of any other charged particle is relatively small compared to that of secondary electrons and incident ions.

The low charging of the isolated electrode during negative-ion implantation is considered to depend on the pulled-back secondary electrons with low energy. In fact, the computer simulation of the trajectory tracing of secondary electrons using the Monte Carlo method[101] has indicated that the secondary electrons with low energy are attracted back to the electrode surface owing to the positively charged electrode. Figure 3.8 shows the deduced process of the charge equilibrium of the negative-ion-implanted isolated electrode for the yield of more than one. At the beginning of ion implantation, the isolated electrode will be positively charged because the yield is larger than one in the ion-energy range above a few keV, as shown in § 2.3 [Fig. 3.8(a)]. As the charging voltage of the electrode increases with positive-charge accumulation, the secondary electrons, starting with those of the lowest energy, will be pulled back to the electrode surface by its positive potential, and hence the yield will apparently decrease [Fig. 3.8(b)]. Eventually,

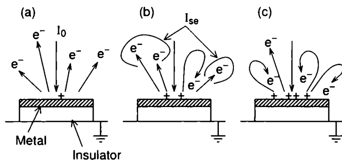

Figure 3.8 Secondary-electron trajectory and positive-charge accumulation on the electrode surface (a) at the beginning of ion implantation ($|I_{se}/I_0| = \gamma > 1$), (b) after brief implantation ($\gamma > |I_{se}/I_0| > 1$), and (c) in the charge equilibrium ($|I_{se}/I_0| = 1$).

the apparent yield will become equal to unity in the charge equilibrium [Fig. 3.8(c)].

Letting the equilibrium charging voltage be V_c, and taking into account the pulled-back secondary electrons with lower energy than the electrode potential of eV_c as shown in Fig. 3.9, we obtain the equilibrium charging-voltage equation:

$$\int_{eV_c}^{E_{max}} N(E)\mathrm{d}E = \frac{1}{\gamma} \tag{3.2}$$

for $\gamma \geq 1$, where E_{max} is the maximum energy of secondary electrons and the definite integral from 0 eV to E_{max} of the energy distribution is normalized to one. Equation (3.2) represents that the ratio of outgoing secondary electrons to all the secondary electrons emitted from the isolated electrode should be equal to $1/\gamma$, and that the charging voltage is given only by two parameters describing secondary electrons, $N(E)$ and γ.

3.3.2 Charging model evaluation

According to eq. (3.2), the charging voltage of the isolated electrode during negative-ion implantation is estimated from the measured data of the energy distribution and the yield of secondary electrons, shown in Chapter 2. The maximum energy, E_{max}, in eq. (3.2) was taken as 40 eV in the measurement range. In the limited energy region, the charging voltage is underestimated and the estimation error increases with the yield and/or the ion energy. In fact, the maximum energy of the ion-induced secondary electrons is approximately 50 eV, and hence the error is less than 1 % and ignorable. The charging voltage estimation was made about Al/glass and Si/glass into which negative carbon ions were implanted.

The estimated charging voltage (closed circles) in negative-carbon-ion implantation into Al/glass is shown in Fig. 3.10, together with the charging voltage measured directly with a high-input-impedance voltmeter (open squares) as a reference. The estimated voltage and the measured voltage are in good agreement with each other. Table 3.1 summarizes the averaged value and the standard deviation of the relative error between the estimated charging voltage and the measured charging voltage, indicating that the estimated and measured voltages agreed within 15 % relative error. This demonstrates

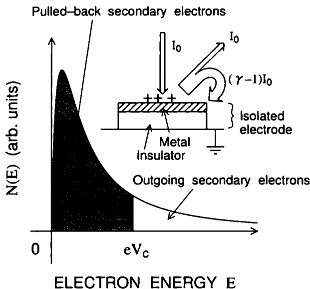

Figure 3.9 Schematic diagram illustrating the charge equilibrium of an isolated electrode during negative-ion implantation. In the charge equilibrium, the negative ions, I_0, are implanted into an isolated electrode; the secondary electrons with an energy of more than eV_c, I_0, move away from it and the others with lower energy, $(\gamma - 1)I_0$, are pulled back to it.

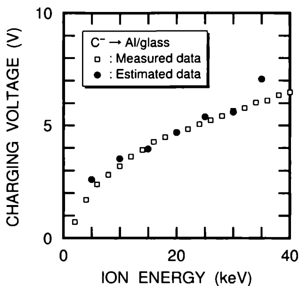

Figure 3.10 Charging voltage estimated using measured data, the energy distribution and the yield, on the basis of eq. (3.2) as a function of ion energy. The charging voltage measured directly with a high-input-impedance voltmeter is plotted together as a reference.

Table 3.1 Averaged value and standard deviation of the relative error between the estimated charging voltage and measured charging voltage.

	Averaged value	Standard deviation
$C^- \rightarrow$ Al/glass	0.077	0.14
$C_2^- \rightarrow$ Al/glass	−0.031	0.097
$C^- \rightarrow$ Si/glass	0.084	0.15
$C_2^- \rightarrow$ Si/glass	−0.061	0.13

that eq. (3.2) is valid.

3.4 Discussion

An estimation of the equilibrium charging voltage from the measured data of the energy distribution and the yield according to eq. (3.2) has indicated quantitative agreement with directly measured charging voltage. In addition, it has been verified that the pulled-back secondary electrons spontaneously cause the equilibrium charging at several volts positive in negative-ion implantation.

The measured charging voltage has indicated the same dependence as that of the yield of secondary electrons on the ion velocity. Let us now consider the relationship between the charging voltage and the yield. Section 2.4 described that the shape of the energy distribution is almost independent of the ion energy. Thus, it is seen from eq. (3.2) that the charging voltage depends only on the yield. Figure 3.11 shows a double-log plot of the energy distribution for 30 keV ion energy of Fig. 2.19. It is observed that a tail extending toward the high-energy region is proportional to electron energy to the power minus two, i.e., $N(E) \propto E^{-2}$. Substituting this relationship into eq. (3.2), we finally obtain the following significant relationship:

$$V_c \propto \gamma. \tag{3.3}$$

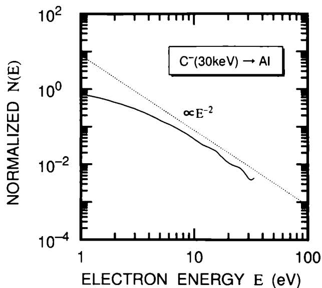

Figure 3.11 Double-log plot of the normalized energy distribution of secondary electrons for 30 keV ion energy of Fig. 2.19. The dotted line indicates the slope of E^{-2}.

The dependence of the directly measured charging voltage on the yield of secondary electrons in negative-carbon-ion implantation into Al/glass is shown in Fig. 3.12. This indicates a good agreement with eq. (3.3). Hence, it is evident that the proportionality of the charging voltage to the yield is due to the feature that the tail of the energy distribution toward the high-energy region is proportional to E^{-2}.

In a series of measurements, a dose of more than 10^{16} ions·cm^{-2} might change the surface conditions of the isolated electrode, such as the work function. When the charging voltage is estimated from the energy distribution obtained in § 2.4, however, the work function of the electrode material is canceled out. This is because the relationships hold as follows. In the charging voltage measurement, there holds the following relationship between the charging voltage, V_c, and the charging voltage measured by the voltmeter, V_c', as shown in Fig. 3.13(a):

$$eV_c + \phi_{sp} = eV_c' + \phi_{sh}, \tag{3.4}$$

where ϕ_{sp} and ϕ_{sh} are the work functions of the electrode material and the shield material, respectively. On the other hand, the relationship between the electron energy, E, and the retarding voltage, V_{ret}, in the energy distribution measurement is, from Fig. 3.13(b), expressed as

$$E + \phi_{sp} = -eV_{ret} + \phi_{ret}, \tag{3.5}$$

where ϕ_{ret} is the work function of the retarding electrode material. Let $E = eV_c$ and assume the corresponding retarding voltage, $V_{ret}|_{E=eV_c}$. Then, eqs. (3.4) and (3.5) lead to

$$V_c' = -V_{ret}|_{E=eV_c} + \frac{\phi_{ret} - \phi_{sh}}{e}. \tag{3.6}$$

In this case, $\phi_{sh} = \phi_{col}$, because the shield and the collector are made of the same material, stainless steel. Equation (3.6) indicates that it is unnecessary to take into account the change of the work function of the electrode material due to the dose. The work function of the retarding electrode to which the gold mesh is attached is 4.58 eV[99], while the work function of the shield (stainless steel) is 4.4 eV[102]. In fact, the voltage difference was ignored because it is as small as the error of the measurement.

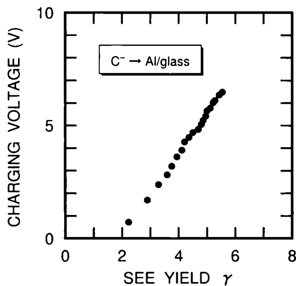

Figure 3.12 Directly measured charging voltage as a function of the yield of secondary electrons.

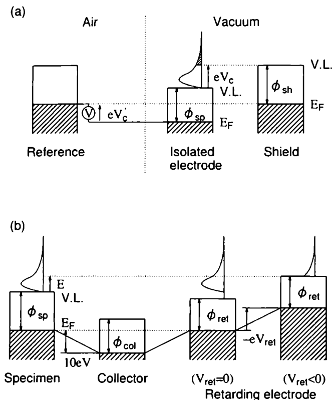

Figure 3.13 Energy diagrams (a) in the charging-voltage measurement, and (b) in the energy distribution measurement.

As described above, the charging mechanism of the negative-ion-implanted isolated electrode is explained only by the behavior of secondary electrons emitted from the electrode in the charge equilibrium. That is, the charging voltage is determined only using the measured yield and energy distribution. Instead of the direct measurement, therefore, we can determine the charging voltage of the isolated electrode from the knowledge of the yield and the energy distribution of secondary electrons. Furthermore, computer simulation on the basis of the charging mechanism will be able to give the charging voltage of complicatedly designed isolated electrodes.

The above model was discussed in the ion current density range below 1 μA$\cdot$cm^{-2}. Beyond 10 μA$\cdot$cm^{-2}, however, a drop of the charging voltage due to the negative beam-potential was observed. Figure 3.14 shows the charging voltage of the isolated electrode in negative-copper-ion implantation at an ion energy of 15 keV. The solid curve denotes the magnitude of the beam potential obtained according to eq. (3.1). The magnitude of the beam potential at an ion current density of 1 mA$\cdot$cm^{-2} is estimated at approximately 300 eV. However, the charging voltage was almost 0 V around 10^{-2} Pa by introducing a xenon gas. This suggests that space charge relaxation results from the neutralization of negative ions and the ionization of xenon particles accompanied with the collision between negative ions and gas particles. Collapse of negative ions is due to large electron detachment cross sections of 10^{-16} 10^{-15} cm^2 even on the order of 10^{-3} Pa[97,98]. Thus, a charging voltage drop due to the negative beam-potential is easily removed by introducing a noble gas.

3.5 Summary

The charging voltage of the isolated electrode during negative-ion implantation was measured under gas pressures of the order of 10^{-4} Pa and dose was 1 5×10^{16} ions$\cdot$cm^{-2}. The measured data have revealed the low, positive charging of the negative-ion-implanted isolated electrode under every condition, except for ion current density of more than a few μA$\cdot$cm^{-2}. Beyond 1 μA$\cdot$cm^{-2}. a voltage drop and negative charging were observed. This

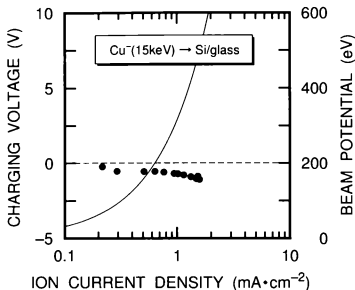

Figure 3.14 Charging voltage of the isolated electrode (Si/glass) as a function of ion current density around 1 $mA \cdot cm^{-2}$ during negative-copper-ion implantation. The solid curve designates the magnitude of beam potential formed by an incident negative-copper-ion beam.

is due to the beam potential. It was demonstrated, however, that introducing a noble gas into the implantation chamber can easily reduce the charge buildup even at high current density beyond 1 $mA{\cdot}cm^{-2}$.

From the measured data of secondary electrons, the charging voltage of the isolated electrode was estimated according to the equilibrium charging-voltage equation. The estimated voltage was in good agreement with the directly measured voltage, proving that the low equilibrium charging of the isolated electrode is achieved in negative-ion implantation. In addition, it has been demonstrated that the slope of the secondary-electron energy distribution determines that the charging voltage is proportional to the yield of secondary electrons.

Finally, the charging phenomena of the isolated electrode in positive-ion, neutral-particle, and negative-ion implantation are summarized. This is based on the charging model described in this chapter. Figure 3.15 shows a comparison between the charging phenomena of the isolated electrode in (a) positive-ion, (b) neutral-particle, and (c) negative-ion implantation. In positive-ion implantation, positive charges inevitably accumulate on the electrode surface whether the emitted secondary electrons are attracted back or not. Thus, the charging voltage will rise up to almost acceleration voltage, V_{acc}. Next, the charge equilibrium in neutral-particle bombardment is accomplished when all the emitted secondary electrons are pulled back to the electrode because of no charges. Therefore, the charging voltage will stay at E_{max}/e, where E_{max} is the maximum energy of secondary electrons induced by neutral particles. In general, the maximum energy of the emitted secondary electrons is approximately 50 eV, and hence the charging voltage will be about 50 V in neutral-particle implantation. The charging voltage of 50 V is not necessarily low in the semiconductor fabrication process, because a 10 nm gate oxide film is damaged by the charging voltage in excess of 10 V. As a consequence, it is concluded that negative-ion implantation is least prone to charging in these three implantation methods.

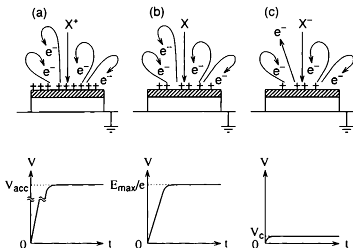

Figure 3.15 Charging diagram of the isolated electrode in (a) positive-ion, (b) neutral-particle, and (c) negative-ion implantation. Each graph below the schematic diagram indicates the charging voltage, V, as a function of implantation time, t.

Chapter 4

The Charging Mechanism of Insulating Materials in Negative-Ion Implantation

4.1 Introduction

As described in Chapter 3, the charging voltage of the isolated electrode is as low as several volts positive during negative-ion implantation up to tens of keV without any external charge neutralization. In addition, the charging voltage remains steady at several volts in the ion current density range below a few $\mu A \cdot cm^{-2}$ and, even above the ion current density, the charging voltage can be kept around 0 V by introducing a noble gas. In the LSI fabrication process, there exists not only the electrically insulated conductive material but also the insulating material, such as the gate and field oxides and photoresist, on the wafer surface. In addition, ion implantation has been utilized for surface modification of the insulating materials, such as glass, polymer, and ceramic[11-17]. Thus, it is necessary to examine the charging phenomenon of the negative-ion-implanted insulating materials as well as isolated electrodes.

It is quite difficult, however, to measure the accurate charging voltage of the negative-ion-implanted insulating material: the implanted and unimplanted regions are not necessarily at the same charging voltage; the surface is not necessarily charged uniformly; a contact with a voltmeter may change the charge distribution on the surface. Accordingly, attention was given to secondary electrons emitted from the insulating surface, and the charging voltage of the surface was deduced from the energy shift in the energy distribu-

tion of secondary electrons. This method was used to study the charging phenomenon of the insulating materials in scanning electron microscope (SEM)[64, 103, 104]: the energy distribution of secondary electrons is assumed to be fixed against a change of the surface potential, then the change of the surface potential will cause the energy shift in the energy distribution. In deducing the charging voltage, in general, attention is given to either true secondary electrons[64, 103] or Auger electrons[104-106]. This study selected the former.

In this chapter, the charging phenomenon of the insulating material during negative-ion implantation is discussed[35, 57-61]. As mentioned above, the charging is evaluated by the energy shift in the energy distribution of secondary electrons emitted from the insulating surface in negative-ion bombardment. Section 2.4 stated the true energy distribution of secondary electrons, which are expected to be emitted from the surface of the *thin* insulator film under almost charging-free conditions. In contrast, the *thick* insulator, through which no charge-compensation current flows, is examined in this chapter. In addition, a charging model based on an electric double layer is proposed to explain the charging phenomenon of the negative-ion-implanted insulating materials in the charge equilibrium.

4.2 Charging voltage estimation by secondary electron energy analysis

4.2.1 Measurement principle

Ion impact on the material surface causes secondary electron emission from the surface as a result of the scattering process in the solid and the surface potential barrier. The emitted secondary electrons have kinetic energies, which is not constant but distributed as shown in § 2.4. This charging voltage measurement is based on a superposition of potential energy on kinetic energy. That is, it is assumed that kinetic energies of secondary electrons emitted from the surface remain fixed irrespective of the surface potential. Then, a change of the surface potential causes the energy shift in the energy distribution.

Figure 4.1 illustrates the measurement principle mentioned above. The contact po-

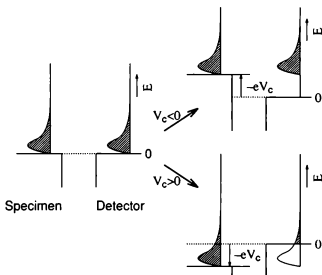

Figure 4.1 Schematic diagram illustrating the measurement principle of the charging voltage by secondary-electron energy analysis. The energy distribution is shifted toward high- or negative-energy region according to the charging of the specimen surface. The contact potential difference between a specimen and a detector is ignored to simplify the figure, because this is not essential.

tential difference between a specimen and a detector is ignored to simplify Fig. 4.1, because the contact potential difference is not essential in this consideration. When the charging voltage of the specimen is V_c, including the sign, a potential energy in terms of electron is expressed as $-eV_c$. At the charging voltage of V_c, the emitted secondary electrons will obtain the potential energy of $-eV_c$: in $V_c < 0$ the secondary electrons will gain the energy and the energy distribution will be shifted toward the high-energy region; in $V_c > 0$, the secondary electrons will lose the energy and the energy distribution will be shifted toward the negative-energy region to the contrary. In the latter case, the energy region of less than 0 eV in the energy distribution cannot be observed using the detector at ground potential. That is, only a shaded portion of the energy distribution shown in Fig. 4.1 is observable.

Taking into account the above consideration, it is likely to estimate the charging voltage from the energy shift in the energy distribution. This is experimentally verified in the following section.

4.2.2 Verification of measurement principle

To verify the measurement principle described in the previous section, the energy distribution of secondary electrons emitted from the biased isolated electrode in negative-ion bombardment was measured.

A 30 mm × 30 mm square isolated electrode, an aluminum film (500 nm) evaporated on a 1.1 mm thick glass plate, was mounted as shown in Fig. 4.2. In this experiment, a hemispherical beam collector was grounded and the isolated electrode was electrically biased varying form −5 V to −20 V in steps of 5 V. In the same manner as the previous measurements, the limiter was at ground potential, while the suppressor was biased by −50 V. Negative carbon ions at an energy of 10 keV with an ion current of 560 nA were implanted into the isolated electrode.

Figure 4.3 shows the normalized energy distributions at the following bias voltage: (a) −5 V, (b) −10 V, (c) −15 V, and (d) −20 V. It is seen from Fig. 4.3 that the shape of the energy distribution is independent of the bias voltage, indicating that the surface

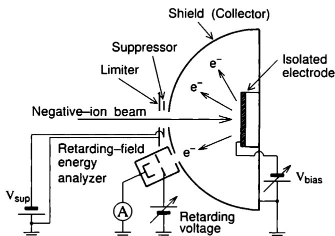

Figure 4.2 Schematic diagram of the measurement apparatus for verifying the measurement principle of the charging voltage by secondary-electron energy analysis. An isolated electrode was negatively biased by $V_{bias}(< 0)$.

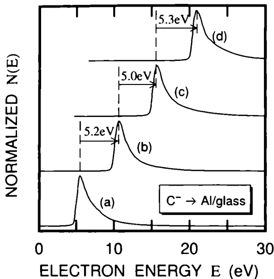

Figure 4.3 Normalized energy distributions of secondary electrons in negative-carbon-ion implantation into the biased aluminum electrode at an ion energy of 10 keV. The biased voltages are as follows: (a) −5 V, (b) −10 V, (c) −15 V, and (d) −20 V.

potential due to the bias voltage does not influence the inherent kinetic energy. The magnitude of the energy shift in the energy distribution increases as the absolute value of the bias voltage is larger. The energy difference between the most probable energies of the adjacent two distributions is as follows: 5.2 eV between (a) and (b); 5.0 eV between (b) and (c); 5.3 eV between (c) and (d). This indicates that the energy shift agrees well with the bias voltage within the relative error of approximately 5 %. This demonstrates that the charging voltage is exactly determined from the energy shift in the measured energy distribution.

4.3 Charging voltage during negative-ion implantation

Section 4.2 has proved that the secondary-electron energy analysis can be used to estimate the charging voltage of the negative-ion-implanted insulating material. This section evaluates the charging of the insulating materials during negative-ion implantation from the results obtained by the energy analysis.

The insulating materials, such as a quartz glass plate and a positive photoresist (OFPR-800) film on silicon substrate, were mounted in the apparatus shown in Fig. 2.14. In this measurement, the specimen surface had no electrical contact and the collector was at the ground potential (V_{ext}=0 V). The other measurement conditions were the same as those in § 2.4. Both specimens are 30 mm × 30 mm square sheets, and the thickness for the quartz glass plate is 1.1 mm; for the photoresist film, 1 μm. The photoresist was neither baked nor developed. Negative carbon ions were implanted into the insulating specimens. No charge-compensation current for both specimens was observed at an ion energy varying 5 keV to 35 keV in the ion current density range from 50 nA·cm^{-2} to 1 μA·cm^{-2}. The energy analysis was carried out varying ion current density and ion energy.

The energy distributions of secondary electrons emitted from the charged insulating materials during negative-ion implantation are described before evaluating the charging

voltage. First, an example of the normalized energy distribution of secondary electrons for the quartz glass is shown in Fig. 4.4. Negative carbon ions were implanted into the quartz glass for the following ion current densities: (a) 60 nA·cm^{-2}, (b) 220 nA·cm^{-2}, and (c) 800 nA·cm^{-2}. All the energy distributions rise around 4 eV, having the most probable energy at 5 eV and a long tail extending toward the high-energy region. It appears that the shape of these energy distributions is close to that for the uncharged insulating material shown in § 2.4.3. However, the most probable energy is larger and the FWHM is slightly larger.

To evaluate the energy distribution for the insulating material charged as a result of negative-ion bombardment, attention was given to two parameters of the most probable energy and the FWHM. Figure 4.5 summarizes the most probable energy and the FWHM of the energy distribution for 10 keV negative-carbon-ion bombardment, as a function of ion current density. The solid symbols and the open symbols designate the most probable energy and the FWHM, respectively. The most probable energy remains steady with respect to the ion current density below 1 μA·cm^{-2}. On the other hand, the FWHM is constant below 200 nA·cm^{-2} but, above it, increases slightly with an approach to 1 μA·cm^{-2}.

Figure 4.6 shows the normalized energy distribution of secondary electrons for the quartz glass at the following carbon-negative-ion energies: (a) 10 keV, (b) 20 keV, and (c) 30 keV. The ion current density was 66-210 nA·cm^{-2}, depending on the ion energy. The broken lines denote the most probable energies of the energy distributions. Figure 4.7 shows the dependence of the most probable energy and the FWHM on the ion energy The figure reflects only the energy dependence, because both of the most probable energy and the FWHM remain steady in the ion current density below 200 nA·cm^{-2}, as shown in Fig. 4.5. On the other hand, Fig. 4.7 shows the most probable energy for both specimens increases with ion energy. This indicates that the energy distribution is shifted toward high-energy region as the ion energy is increased. It appears that the FWHM increases slowly with the incident ion energy.

The charging voltage estimation for the negative-ion-implanted insulating material

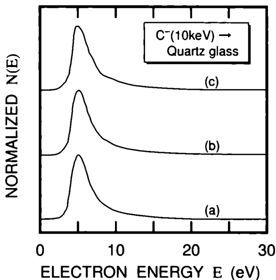

Figure 4.4 Normalized energy distributions of secondary electrons during negative-carbon-ion implantation into quartz glass for three different ion current densities: (a) 60 $nA \cdot cm^{-2}$, (b) 220 $nA \cdot cm^{-2}$, and (c) 800 $nA \cdot cm^{-2}$.

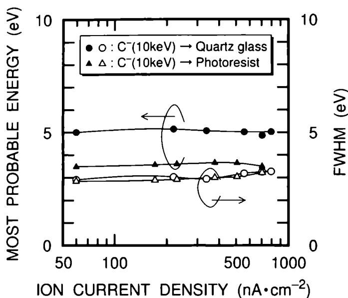

Figure 4.5 Most probable energy and FWHM of the energy distribution of secondary electrons emitted from quartz glass and photoresist during negative-carbon-ion implantation as a function of ion current density.

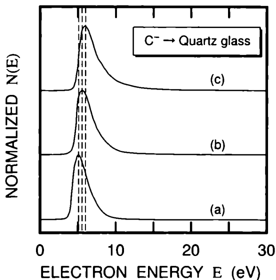

Figure 4.6 Normalized energy distributions of secondary electrons during negative-carbon-ion implantation into quartz glass for three different ion energies: (a) 10 keV, (b) 20 keV, and (c) 30 keV. The broken lines denote the most probable energies of the energy distributions.

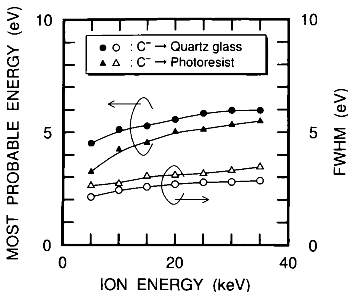

Figure 4.7 Most probable energy and FWHM of the energy distribution of secondary electrons emitted from quartz glass and photoresist in negative-carbon-ion implantation as a function of ion energy.

is made according to the principle verified in § 4.2. The results shown in Fig. 4.7 indicate the changes of the relative values in the charging voltage, not the absolute values. The absolute value can be estimated by reference to the energy distribution of secondary electrons from the thin, uncharged SiO_2 film obtained in § 2.4.3, in comparison between the most probable energies. The charging voltage estimation for the photoresist film also used the data for this thin SiO_2 film as a reference, because there is no data on the energy distribution from the thin, uncharged photoresist film owing to no charge-compensation current enough to reduce the charging. Thus, the estimation for photoresist rests on the assumption that the energy distribution for the uncharged photoresist is the same as for the uncharged SiO_2.

Figure 4.8 shows the estimated charging voltage of the insulating specimens during negative-carbon-ion implantation as a function of ion energy. This indicates that the charging voltage is negative and decreases gradually with increasing ion energy. However, the absolute value is as low as several volts in the ion energy region below 40 keV. This demonstrates that negative-ion implantation is less prone to charging for the insulating material as well as for the isolated electrodes.

4.4 Modelling of negative-ion-implanted insulating materials

4.4.1 Charging model based upon electrical double layer

It has been revealed by using the secondary-electron energy analysis that the insulating materials during negative-ion implantation are negatively charged. In addition, it has been found out that the absolute value of the charging voltage increases gradually with ion energy. These features are different from that for the negative-ion-implanted isolated electrode discussed in Chapter 3. This indicates that the charging model for the negative-ion-implanted isolated electrode discussed in § 3.3 does not apply to the case of the insulating materials during negative-ion implantation. Therefore, this section describes the charging model of the negative-ion-implanted insulating material.

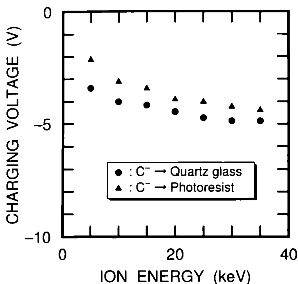

Figure 4.8 Charging voltage of the negative-carbon-ion-implanted quartz glass and photoresist as a function of ion energy. This data is estimated by reference to the energy distribution of secondary electrons emitted from the thin, uncharged SiO_2 film.

In ion impact on the insulation materials, there occurs dielectric polarization because of a low electron-hole recombination originating from the very low charge mobility in the insulating material, unlike the conductive material. As a result, the inner electric field deriving from dielectric polarization can influence the secondary electron emission. Thus, a simplified charging model of the insulating material during negative-ion implantation was considered. This model is based on an electric double layer, shown in Fig. 4.9. In the figure, the thickness of the electric double layer is emphasized but, in fact, it can be predicted that it is on the order of the projected range of the incident ions.

The formation of the electric double layer is considered as follows. At the beginning of implantation, the positive charges will be dominant inside the material because the yield of secondary electrons is larger than one in the ion energy range above a few keV as shown in § 2.3.4. As a result of the low level of charge recombination, the excited electrons will be affected by an inner electric field and then stay at the trap level around the surface layer. Accordingly, the charges will be distributed as follows: a negatively charged layer due to the secondary electrons which fail to escape and stay around the top surface layer; a positively charged layer which results from the absence of electrons inside the insulator. With an increase in dose, the inner electric field, or a potential barrier at the surface will increase to prevent the secondary electrons from ejecting. Thus, an excess electron emission is suppressed by increasing the potential barrier, so that the apparent yield of secondary electrons is reduced. Eventually, the apparent yield will approach to unity in the charge equilibrium. The formation process is shown in Fig. 4.10. On the contrary, the excess potential barrier suppresses the emission and increases the excited electrons staying inside the material. As a result, the electron-hole recombination increases, and hence the electric field is decreased and the escaping electrons are increased. That is, the electric double layer is considered to play a role of a gate to make the yield equal to one in the charge equilibrium.

A more detailed discussion on the charging model will be provided below. It is assumed that the secondary electrons escaping to a vacuum originate from an excitation from the top of the valence band. Then, the energy distribution at the initial stage of

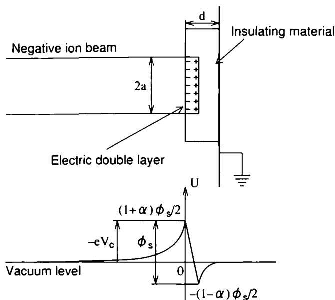

Figure 4.9 Charging model of the negative-ion-implanted insulating material (electric-double-layer model) and its energy diagram.

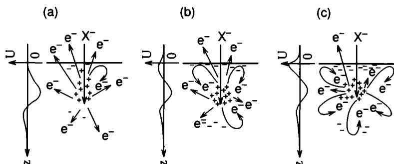

Figure 4.10 Schematic model illustrating the formation process of an electrical double layer in the vicinity of the insulating surface in negative-ion impact: (a) at the beginning of ion implantation, (b) after brief implantation, and (c) in the charge equilibrium. Each graph beside the schematic model indicates the potential energy, U, as a function of depth, z.

implantation, $N(E)$, will be written as[69]

$$N(E) \propto \frac{1}{(E+E_i)^2} \cdot \frac{E}{E+E_i}, \tag{4.1}$$

where E denotes the kinetic energy of the secondary electron measured from the vacuum level and E_i is the ionization energy. The first factor in eq. (4.1) is proportional to the number of the secondary electrons excited in the insulating material[69, 107]; the second factor is a transmission coefficient in the direction normal to the surface[69].

As described above, an increase in dose forms the surface barrier. This barrier is designated a surface potential, ϕ_s. The surface potential is defined as the potential difference between the positively and the negatively charged layers, as shown in Fig. 4.9. The energy levels at the positively charged layer and the negatively charged layer are given by an electric image method as $-(1-\alpha)\phi_s/2$ and $(1+\alpha)\phi_s/2$, respectively. The parameter, α, is expressed in terms of the thickness of the insulating material, d, and the ion-beam diameter, $2a$: $\alpha = 1 - 2d/\sqrt{a^2+(2d)^2}$. The energy shift, $-eV_c$, resulting from the charging as shown in Fig. 4.9, is observed by the energy analysis. Accordingly, the energy distribution in the charge equilibrium, $N_c(E)$, is as follows:

$$N_c(E) \propto \frac{1}{[E+E_i+(1-\alpha)\phi_s/2]^2} \cdot \frac{E-(1+\alpha)\phi_s/2}{E+E_i-(1+\alpha)\phi_s/2}. \tag{4.2}$$

Since incoming charges (negative ions) become equal to outgoing charges (secondary electrons with high energy) in the charge equilibrium, we obtain the following equilibrium equation:

$$\frac{\int_{(1+\alpha)\phi_s/2}^{E_{max}} N_c(E)\mathrm{d}E}{\int_0^{E_{max}} N(E)\mathrm{d}E} = \frac{1}{\gamma}, \tag{4.3}$$

where γ is the yield of secondary electrons and E_{max} is the maximum energy of secondary electrons. In addition to the assumption of $E_{max} \to \infty$, $\alpha=1$ is assumed to simplify the expression, deriving from the assumption that the thickness is small enough compared with the beam diameter, $d/a \ll 1$. Then, eq. (4.3) reduces to

$$-\left(\frac{E_i}{\phi_s}\right)^2 \ln\frac{E_i+\phi_s}{E_i} + \frac{E_i}{\phi_s} = \frac{1}{2\gamma}. \tag{4.4}$$

Under the above assumptions, $-eV_c$ will become equal to ϕ_s. In the following section, therefore, a discussion is continued after a substitution of $-eV_c$ for ϕ_s.

4.4.2 Charging model evaluation

Now, the relationship between $-eV_c$ and the most probable energy of $N_e(E)$, E_p, is easily obtained from eq. (4.2),

$$-eV_c = \frac{2E_p + E_i - \sqrt{2E_pE_i + 3E_i^2}}{2}. \tag{4.5}$$

Expansion of eqs. (4.4) and (4.5) to the first approximation in a Taylor series leads to the following simple expression:

$$V_c \simeq E_i(A\gamma + B), \tag{4.6}$$

$$E_p \simeq E_i(A'\gamma + C). \tag{4.7}$$

We see that both V_c and E_p are almost proportional to γ, because any variation in A, A', B, and C to γ is within approximately 5% for $2 \leq \gamma \leq 6$. In fact, A' is larger by 10 % than A. Hence, the charging voltage estimated from the most probable energy of the energy distribution is overestimated. Nevertheless, it is rather difficult to determine the lowest energy of the energy distribution because of the tail toward negative-energy region.

Figure 4.11 shows the charging voltage as a function of the yield of secondary electrons in negative-carbon-ion implantation into quartz glass. The yield proportionality to ion velocity at 10^5 m·s^{-1} order, as stated in § 2.3.4, was linked to Fig. 4.8. It is clear that the charging voltage is proportional to the yield. The low-magnitude, negative charging of the insulating material during negative-ion implantation is likely to be caused by the formation of the electric double layer around the top layer in the charge equilibrium.

4.5 Discussion

The consideration in the previous section did not include the thickness of the electric double layer to be taken into account. The thickness is discussed below, assuming a carbon-ion impact on a silicon-dioxide target.

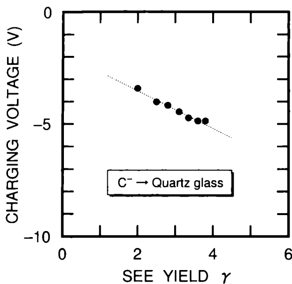

Figure 4.11 Charging voltage as a function of the yield in negative-carbon-ion implantation into quartz glass.

The ions penetrate into the material while transferring the energy to the target electrons and losing their energy. This transferred energy originates from the electronic stopping power. Put the electronic transferred energy $E_t(z)$. Then, the number of the excited electrons at a depth of z from the surface, $N_{ex}(z)$, is given by

$$N_{ex}(z) = \frac{E_t(z)}{J} N_d, \tag{4.8}$$

where N_d is the number of the incident-ion density per a second. According to the three step model introduced in § 2.2, the excited electrons after scattering are distributed as follows:

$$N^*_{ex}(z) = \int_0^d N_{ex}(s) \frac{1}{2L} \exp\left(-\frac{|z-s|}{L}\right) ds. \tag{4.9}$$

As a result, the charge-density distribution after the excited-electron redistribution, $\rho(z)$, is expressed as

$$\rho(z) = e[N_{ex}(z) - N^*_{ex}(z)]. \tag{4.10}$$

This charge-density distribution provides the thickness of the electric double layer.

Figure 4.12 shows the transferred energy as a function of a depth from the surface. The transferred energy originates from both projectiles and recoil atoms. The broken curve designates the result calculated by TRIM[92] under the condition of 10 keV carbon-ion impact on the silicon-dioxide target. The solid curve is written as

$$E_t(z) = E_{t0} \exp\left(-\left|\frac{z - D_p}{D}\right|^2\right), \tag{4.11}$$

where E_{t0}, D, and D_p are 170 eV·nm^{-1}·ion^{-1}, 23 nm, and 13 nm, respectively. The approximate curve expressed in eq. (4.11) was used to obtain the charge-density distribution. Figure 4.13 shows the absolute value of the charging density, calculated using the value listed in Table 4.1. The figure indicates the formation of an electric triple layer: a negatively charged top layer, a positively charged layer inside the material, and a negatively charged layer further inside. The thickness of the electric double layer on the surface side is approximately 30 nm. This is almost equal to the full width at half-maximum of the transferred energy.

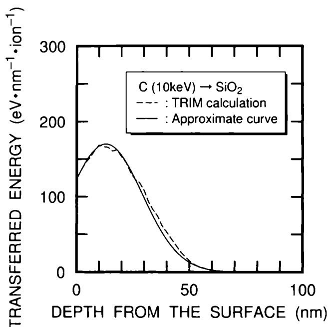

Figure 4.12 Transferred energy functions due to carbon ions incident on silicon dioxide obtained by TRIM calculation, originating from both projectile and recoil atoms. The approximate curve was used for the model calculation.

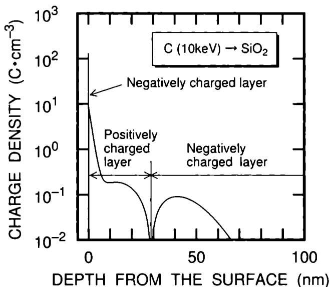

Figure 4.13 Charge-density distribution after the excited-electron redistribution, calculated by using data shown in Table 4.1. The charge density is shown with the absolute value.

Table 4.1 Values of the parameters used to calculate the charge-density distribution.

Parameter	Value	Unit
d	200	nm
D	23	nm
D_p	13	nm
L	1.4	nm
J	50[†]	eV
N_d	5×10^{12}	ions·cm^{-2}·s^{-1}
E_{i0}	170	eV·nm^{-1}·ion^{-1}

[†]This value derives from ref. 87.

Next, the potential and the electric field inside the silicon dioxide during negative-carbon-ion implantation was calculated by using the charge-density distribution shown in Fig. 4.13. In addition, the one-dimensional model shown in Fig. 4.14 was introduced and a calculation was made by using the finite element method (FEM), applying the Neumann boundary condition to the insulating surface and the Dirichlet boundary condition to the rear boundary. The values of the parameters used to calculate are listed in Table 4.2. In the table, D_s and ε_r are the distance from the insulating surface to the shield and the relative permittivity of the insulating material, respectively. The result is shown in Fig. 4.15, indicating that the potential barrier with respect to the electron is formed close to the surface. As described above, it is considered that this potential barrier controls secondary electron emission and permits only the excited electrons with a high energy to escape into a vacuum.

Since this potential barrier is due to the electric double layer formed around the surface, it can be considered that this charging model is suitable to be designated an electric double layer rather than an electric triple layer. Such a double layer model was

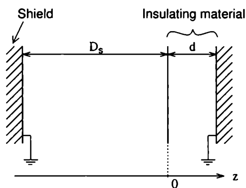

Figure 4.14 One-dimensional model introduced to calculate the potential and the electric field inside the insulating material from the charge-density distribution after the excited-electron redistribution.

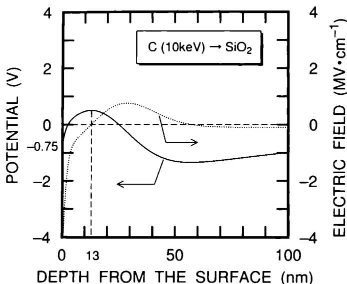

Figure 4.15 Potential and electric field inside the insulating material calculated from the charge-density distribution after the excited-electron redistribution in one-dimensional model by using data shown in Tables 4.1 and 4.2.

Table 4.2 Values of the parameters used to calculate the potential and the electric field.

Parameter	Value	Unit
d	200	nm
D_s	100	mm
ε_r	2.7	

proposed in electron irradiation onto the insulating material[106]. This is the same case about the polarity of the projectile as negative-ion implantation.

4.6 Summary

To estimate the charging voltage of the insulating material during negative-carbon-ion implantation, the energy distribution of secondary electrons emitted from the charged surface was measured. As a result, the energy shift toward the high-energy region with increasing ion energy was observed. This indicates the charging voltage decreases with increasing ion energy. Furthermore, the charging voltage of the insulating material was evaluated in comparison with the energy distribution of the uncharged insulating material, a thin oxide film. As a consequence, it has been evident that the charging voltage is negative and the absolute value increases in proportion to the yield of secondary electrons. On the other hand, the dependence of the ion current density was not observed below 1 μA$\cdot$cm^{-2}.

Furthermore, a simplified charging model based on an electric double layer, which plays a role of a gate to make the yield equal to one in the charge equilibrium, was proposed to examine the negative charging of the insulating material during negative-ion implantation. This model has explained the charging properties qualitatively and suggested that the energy shift toward the high-energy region is due to the escape of only the excited electrons with higher energy by the potential barrier. In addition, it has

been found that the thickness of the electric double layer is approximately a few tens of nm and that the width of the potential barrier is associated with the transferred energy distribution.

Chapter 5

Conclusions

Negative-ion implantation is intrinsically less prone to charging unlike conventional ion implantation, namely, positive-ion implantation. To utilize the benefit effectively it is important to understand the charging phenomenon in negative-ion implantation into the insulating or the insulated materials. This is the primary purpose of this research. The other purpose of this study is to examine secondary electron emission induced by negative ions, because secondary electrons are related closely to the charging. To apply the results to ion implantation in semiconductor fabrication, all measurements were carried out under the residual gas pressures of 10^{-4} Pa order and a dose of 10^{16} ions·cm^{-2}.

In Chapter 2, secondary electron emission induced by negative ions was discussed. The significant parameters representing the secondary electron emission, i.e., the yield and the energy distribution, were measured for the conductive and the insulating materials. The measurement for the insulating material was carried out by using a thin oxide film and low ion current at room temperature to minimize the charge buildup on the surface. The measured data have indicated the same properties irrespective of the conductivity of the target material.

The results for the yield measurement have indicated the yield proportionality to ion velocity in the velocity region of 10^5 to 10^6 m·s^{-1}. This has demonstrated that the secondary electron emission induced by negative ions as well as by positive ions is mainly the kinetic mechanism. In addition, it has been discovered that the yield for negative-ion bombardment is larger by one unit than that for positive-ion bombardment. It is considered that the yield larger by one unit is due to the detachment of an extra electron bound

to a negative ion in ion impact on a solid surface. Therefore, the negative-ion-induced secondary electrons consists of this extra electron and the electron originating from kinetic emission. In kinetic emission a part of electrons excited by a series of collisional events among incident ions and recoil atoms can reach the surface of the solid and escape. As a result, the energy distribution has a few eV peak and a long tail extending toward the high-energy region. No other peak, such as an Auger peak, was observed in the measured energy distribution. These two parameters were independent of ion current but depended somewhat on target materials in negative-ion irradiation at tens of keV with an ion current density of less than a few $\mu A \cdot cm^{-2}$.

Almost all measurements were carried out by using negative carbon ions except for a few measurements of the yield. However, the above properties are considered to apply to all combinations between negative ions and target materials because the secondary electron emission phenomenon originates from kinetic events inside target material.

The charging of an electrically insulated conductive material, which is designated an isolated electrode, during negative-ion implantation without any charge compensation was investigated in Chapter 3. The experimental result has revealed the positive, low charging of the negative-ion-implanted isolated electrodes under any conditions, except for ion current density of more than a few $\mu A \cdot cm^{-2}$. In the ion current density range below 1 $\mu A \cdot cm^{-2}$, it has been found that the charging voltage of the isolated electrodes increases in proportion to ion velocity and the value is still 6–8 V even at an ion energy of 40 keV. In addition, it has been shown that the charging voltage remains steady, independent of ion current density.

Beyond 1 $\mu A \cdot cm^{-2}$, a voltage drop with increasing ion current density and the negative charging were observed. This is due to the beam potential resulting from space charge of the incident negative ions. It was found, however, that introducing a noble gas into the implantation chamber can easily remove this effect of the beam potential even at high current density of more than 1 $mA \cdot cm^{-2}$. This results from the neutralization of negative ions and the ionization of noble gas particles accompanied with the collisions between negative ions and gas particles.

Taking into account the behavior of the emitted secondary electrons in the steady state, an equilibrium charging-voltage equation was presented. The equation is expressed only by the yield and the energy distribution of secondary electrons. To verify the equilibrium charging-voltage equation, the charging voltage of the negative-ion-implanted isolated electrode was estimated from the measured data of secondary electrons. The estimated voltage has showed good agreement with the directly measured charge, and hence it has been revealed that the low equilibrium-charging in negative-ion implantation is achieved owing to the low-energy secondary electrons pulled back to the electrode. In addition, it has been demonstrated that the slope of the energy distribution extending toward the high-energy region determines that the charging voltage is proportional to the yield.

Chapter 4 described the charging phenomenon of the insulating materials during negative-ion implantation. The implanted and unimplanted regions on the insulating surface are not necessarily charged uniformly, and therefore it is difficult to measure the charging voltage using a voltmeter. Hence, the charging voltage measurement for the negative-ion-implanted insulating materials was carried out by secondary-electron energy analysis. This is based on the phenomenon that the energy shift in the energy distribution is associated closely with the surface charging. The preliminary experiment using the biased isolated electrode has indicated that the energy shift agreed fairly well with the voltage applied to the electrode.

Indeed, the energy distribution measurement of secondary electrons emitted from the charged insulating materials during negative-carbon-ion implantation has showed the energy shift toward the high-energy region with increasing ion energy. This energy shift indicates that the charging voltage decreases with increasing ion energy. A charging voltage estimation of the insulating material was done in comparison with the energy distribution of the uncharged insulating material, i.e., a thin oxide film. As a consequence, it has been discovered that the charging voltage is negative and the absolute value increases almost in proportion to the yield of secondary electrons. In addition, it has been demonstrated that the magnitude is as low as several volts in carbon-ion bombardment below 40 keV.

To examine the negative charging of the insulating materials during negative-ion implantation, a simplified charging model based on an electric double layer was proposed. This model has explained the charging properties qualitatively. It has become evident from the model that the energy shift toward the high-energy region results from the increase in the potential barrier permitting the escape of only the excited electrons with higher energy.

This study has obtained knowledge on negative-ion-induced secondary electron emission through the measurement of the secondary electrons emitted from the materials. Furthermore, the charging mechanism of the insulating or the insulated materials during negative-ion implantation has been understood through the study of the secondary electrons. As a consequence, an intimate relationship between the emitted secondary electrons and the charging of the insulating or the insulated materials during negative-ion implantation was confirmed. In addition, it has been verified that the negative-ion implantation is inherently less prone to charging. This study should be useful for charging-free implantation into the insulating or the insulated materials by using negative ions in future LSI and TFT fabrication, surface modification, etc.

References

[1] R. S. Ohl: Bell Syst. Tech. J. **31** (1952) 104.

[2] S. Moffatt: Nucl. Instrum. & Methods Phys. Res. **B96** (1995) 1.

[3] S. Nanba: *Ion Chunyu Gijutsu* (Ion Implantation Technology) (Kogyochosa-kai, Tokyo, 1979) 2nd ed., Chap. 1, p. 1 [in Japanese].

[4] T. Ito, T. Tsurushima, K. Yata and I. Oodomari: *Ion Inpuranteshon riron to oyo* - (Ion Implantation - Theories and Applications -) (Shokodo, Tokyo, 1976) 1st ed., Chap. 1, p. 1 [in Japanese].

[5] W. Schockley: U. S. Patent 2666814 (1954).

[6] W. Schockley: U. S. Patent 2787564 (1957).

[7] R. S. Ohl: U. S. Patent 2750541 (1956).

[8] J. W. Mayer: U. S. Patent 2842466 (1958).

[9] J. H. Freeman: Nucl. Instrum. & Methods **22** (1963) 306.

[10] W. Mari: *Zusetsu cho-LSI kogaku* (Illustration ULSI Engineering) (Keigaku-shuppan, Tokyo, 1990) p. 179 [in Japanese].

[11] T. Venkatesan: Nucl. Instrum. & Methods Phys. Res. **B7/8** (1985) 461.

[12] J. D. Carlson, J. E. Bares, A. M. Guzman and P. P. Pronko: Nucl. Instrum. & Methods Phys. Res. **B7/8** (1985) 507.

[13] P. Sioshansi: Nucl. Instrum. & Methods Phys. Res. **B19/20** (1987) 204.

[14] Y. Suzuki, M. Kusakabe, M. Iwaki and M. Suzuki: Nucl. Instrum. & Methods Phys. Res. **B32** (1988) 120.

[15] G. Marletta: Nucl. Instrum. & Methods Phys. Res. **B46** (1990) 295.

[16] J. P. Biersack and R. Kallweit: Nucl. Instrum. & Methods Phys. Res. **B46** (1990) 309.

[17] Y. Suzuki, M. Kusakabe, J.-S. Lee, M. Kaibara, M. Iwaki and H. Sasabe: Nucl. Instrum. & Methods Phys. Res. **B65** (1992) 142.

[18] F. Iacona and G. Marletta: Nucl. Instrum. & Methods Phys. Res. **B65** (1992) 50.

[19] G. Mondio, F. Neri, S. Patanè, A. Arena, G. Marletta and F. Iacona: Thin Solid Films **207** (1992) 313.

[20] S. Miyamoto, A. Ohashi, J. Kimura, S. Tobe and T. Akaike: Sensors & Actuators **13-14** (1993) 196.

[21] S. Durbach, J. Mellor, N. J. Covile and T. E. Derry: Nucl. Instrum. & Methods Phys. Res. **B80/81** (1993) 294.

[22] M. Heuberger, R. Telle and G. Petzow: Nucl. Instrum. & Methods Phys. Res. **B80/81** (1993) 1040.

[23] H. Tsuji, H. Itoh, Y. Toyota, S. Nagumo, Y. Gotoh and J. Ishikawa: *Proc. 5th Symp. Beam Engineering of Advanced Material Syntheses, Tokyo, 1994* (Ionics, Tokyo, 1994) p. 185 [in Japanese].

[24] M. E. Mack, G. Ryding, D. H. Douglas-Hamilton, K. Steeples, M. Farley, V. Gillis, N. White, A. Wittkower and R. Lambracht: Nucl. Instrum. & Methods Phys. Res. **B6** (1985) 405.

[25] V. K. Basra, C. M. McKenna and S. B. Felch: Nucl. Instrum. & Methods Phys. Res. **B21** (1987) 360.

[26] N. Aoki, K. Ishikawa, T. Namura, Y. Fukuzaki, G. Fuse, M. Yoshida and M. Inoue: Nucl. Instrum. & Methods Phys. Res. **B74** (1993) 306.

[27] B. En and N. W. Cheung: Nucl. Instrum. & Methods Phys. Res. **B74** (1993) 311.

[28] M. Kobayashi and S. Nagajima: *VLSI Purosesu Gijutsu* (VLSI Process Technology) (Nikkankogyo-shinbunsha, Tokyo, 1993) Chap. 3, p. 55 [in Japanese].

[29] D. L. Smatlak, M. E. Mack and S. Mehta: Nucl. Instrum. & Methods Phys. Res. **B96** (1995) 22.

[30] H. Ito, T. Kamata, J. England, I. Fotheringham, F. Plumb and M. I. Current: Nucl. Instrum. & Methods Phys. Res. **B96** (1995) 30.

[31] M. E. Mack, P. Barschall, P. Corey, S. Satoh and S. Walther: Nucl. Instrum. & Methods Phys. Res. **B74** (1993) 287.

[32] W. Lukaszek, W. Dixon, E. Quek, W. Weisenberger and H. Sung: Nucl. Instrum. & Methods Phys. Res. **B74** (1993) 301.

[33] V. E. Krohn, Jr.: J. Appl. Phys. **33** (1962) 3523.

[34] J. Ishikawa: Rev. Sci. Instrum. **63** (1992) 2368.

[35] J. Ishikawa, H. Tsuji, Y. Toyota, Y. Gotoh, K. Matsuda, M. Tanjyo and S. Sakai: Nucl. Instrum. & Methods Phys. Res. **B96** (1995) 7.

[36] M. Mueller and G. Hortig: IEEE Tran. Nucl. Sci. **NS-16** (1969) 38.

[37] R. Middleton: Nucl. Instrum. & Methods **118** (1974) 329.

[38] H. H. Anderson and P. Tykesson: IEEE Tran. Nucl. Sci. **NS-22** (1975) 16332.

[39] R. Middleton: Nucl. Instrum. & Methods Phys. Res. **A220** (1984) 104.

[40] G. D. Alton, Y. Mori, A. Takagi, A. Ueno and S. Fukumoto: Rev. Sci. Instrum. **61** (1990) 372.

[41] J. Ishikawa, Y. Takeiri, H. Tsuji, T. Taya and T. Takagi: Nucl. Instrum. & Methods Phys. Res. **232** (1984) 186.

[42] J. Ishikawa, Y. Takeiri and T. Takagi: Rev. Sci. Instrum. **57** (1986) 1512.

[43] J. Ishikawa, H. Tsuji and T. Takagi: Vacuum **36** (1986) 887.

[44] J. Ishikawa, H. Tsuji, Y. Okada, M. Shinoda and Y. Gotoh: Vacuum **44** (1993) 203.

[45] J. Ishikawa: Rev. Sci. Instrum. **65** (1994) 1290.

[46] J. Lindhard and M. Scharff: Phys. Rev. **124** (1961) 128.

[47] J. Ishikawa and H. Tsuji: Nucl. Instrum. & Methods Phys. Res. **B74** (1993) 118.

[48] S. Sakai, M. Tanjyo, K. Matsuda, Y. Gotoh, H. Ohnishi, H. Tsuji and J. Ishikawa: *Proc. 9th Int. Conf. Ion Implantation Technology, Gainesville, 1992* (North-Holland, Amsterdam, 1993) p. 617.

[49] Y. Toyota, H. Tsuji, Y. Gotoh and J. Ishikawa: Jpn. J. Appl. Phys **34** (1995) 6487.

[50] Y. Toyota, H. Honda, H. Tsuji, Y. Gotoh and J. Ishikawa: J. Vac. Soc. Jpn. **38** (1995) 796 [in Japanese].

[51] S. Ikeda, Y. Toyota, H. Tsuji, Y. Gotoh and J. Ishikawa: *Proc. 6th Symp. Beam Engineering of Advanced Material Syntheses, Tokyo, 1995* (Ionics, Tokyo, 1995) p. 175 [in Japanese].

[52] Y. Toyota, H. Tsuji, Y. Gotoh and J. Ishikawa: submitted to Jpn. J. Appl. Phys.

[53] H. Tsuji, S. Sakai, Y. Okayama, Y. Toyota, Y. Gotoh, M. Tanjyo, K. Matsuda and J. Ishikawa: J. Vac. Soc. Jpn. **37** (1994) 135 [in Japanese].

[54] Y. Toyota, H. Tsuji, S. Nagumo, S. Sakai, Y. Gotoh, J. Ishikawa and K. Matsuda: J. Vac. Soc. Jpn. **38** (1995) 224 [in Japanese].

[55] Y. Toyota, Y. Okayama, H. Tsuji, Y. Gotoh, J. Ishikawa, S. Sakai, M. Tanjyo and K. Matsuda: *Proc. 4th Symp. Beam Engineering of Advanced Material Syntheses, Tokyo, 1993* (Ionics, Tokyo, 1993) p. 75 [in Japanese].

[56] Y. Toyota, H. Tsuji, S. Nagumo, C. Ichihara, S. Sakai, Y. Gotoh and J. Ishikawa: *Proc. 5th Symp. Beam Engineering of Advanced Material Syntheses, Tokyo, 1994* (Ionics, Tokyo, 1994) p. 209 [in Japanese].

[57] H. Tsuji, Y. Toyota, S. Nagumo, Y. Gotoh, J. Ishikawa, S. Sakai, M. Tanjyo and

K. Matsuda: J. Vac. Soc. Jpn. **37** (1994) 139 [in Japanese].

[58] H. Tsuji, Y. Toyota, J. Ishikawa, S. Sakai, Y. Okayama, S. Nagumo, Y. Gotoh and K. Matsuda: *Proc. 10th Int. Conf. Ion Implantation Technology, Catania, 1994* (North-Holland, Amsterdam, 1995) p. 612.

[59] H. Tsuji, S. Nagumo, Y. Toyota, Y. Gotoh and J. Ishikawa: J. Vac. Soc. Jpn. **38** (1995) 221 [in Japanese].

[60] Y. Toyota, H. Tsuji, S. Nagumo, Y. Gotoh and J. Ishikawa: to be published in Appl. Surf. Sci.

[61] S. Nagumo, Y. Toyota, H. Tsuji, Y. Gotoh, J. Ishikawa, S. Sakai, M. Tanjyo and K. Matsuda: *Proc. 4th Symp. Beam Engineering of Advanced Material Syntheses, Tokyo, 1993* (Ionics, Tokyo, 1993) p. 79 [in Japanese].

[62] J. Devooght, J.-C. Dehaes, A. Dubus, M. Cailler, J.-P. Ganachaud, M. Rösler and W. Brauer: *Particle Induced Electron Emission I*, ed. G. Höhler (Springer-Verlag, Heidelberg, 1991) 1st ed., Vol. 122.

[63] E. S. Parilis, F. F. Umarov, L. M. Kishinevsky, V. K. Verleger, N. Y. Turaev, S. L. Nizhnaya, B. E. Baklitzky and I. S. Bitensky: *Atomic Collisions on Solid Surfaces* (North-Holland, Amsterdam, 1993) Chap. 11, p. 391.

[64] H. Seiler: J. Appl. Phys. **54** (1983) R1.

[65] R. Bindi, H. Lanteri and P. Rostaing: Scanning Microsc. **1** (1987) 1475.

[66] J. Schou: Scanning Microsc. **2** (1988) 607.

[67] A. J. Dekker: Solid State Phys. **6** (1958) 251.

[68] H. Seiler: Z. Angew. Phys **22** (1967) 249.

[69] M. P. Seah: Surf. Sci. **17** (1969) 132.

[70] J. Schou: Phys. Rev. B **22** (1980) 2141.

[71] C. Benazeth, P. Cafarelli and N. Benazeth: Nucl. Instrum. & Methods Phys. Res. **B62** (1991) 47.

[72] K. H. Krebs: Vacuum **33** (1983) 555.

[73] D. Hasselkamp, S. Hippler and A. Scharmann: Nucl. Instrum. & Methods Phys. Res. **B18** (1987) 561.

[74] B. Hird, C. Pepin and G. Kelly: J. Appl. Phys. **56** (1984) 3304.

[75] H. D. Hagstrum: Phys. Rev. **96** (1954) 325.

[76] H. D. Hagstrum: Phys. Rev. **96** (1954) 336.

[77] L. M. Kishinevskii: Radiat. Eff. (1973) 23.

[78] E. J. Sternglass: Phys. Rev. **108** (1957) 1.

[79] E. S. Parilis and L. M. Kishinevskii: Sov. Phys.-Solid State **3** (1960) 885.

[80] A. Dubus, J. Devooght and J. C. Dehaes: Nucl. Instrum. & Methods Phys. Res. **B13** (1986) 623.

[81] R. A. Baragiola, E. V. Alonso and A. Oliva-Florio: Phys. Rev. B **19** (1979) 121.

[82] A. Clouvas, A. Katsanos, B. Farizon-Mazuy, M. Farizon, M. J. Gaillard and S. Ousakit: Phys. Rev. B **48** (1993) 6832.

[83] G. Holmén, B. Svensson, J. Schou and P. Sigmund: Phys. Rev. B **20** (1979) 2247.

[84] E. V. Alonso, R. A. Baragiola, J. Ferrón and A. Oliva-Florio: Phys. Rev. B **22** (1980) 80.

[85] H. Rothard, K. Kroneberger, A. Clouvas, E. Veje, P. Lorenzen, N. Keller, J. Kemmler, W. Meckbach and K.-O. Groeneveld: Phys. Rev. A **41** (1990) 2521.

[86] A. Clouvas, A. Katsanos, B. Farizon-Mazuy, M. Farizon and M. J. Gaillard: Phys. Rev. B **43** (1991) 2496.

[87] R. J. Beuhler and L. Friedman: J. Appl. Phys. **48** (1977) 3928.

[88] J. Ishikawa, Y. Takeiri and T. Takagi: Rev. Sci. Instrum. **55** (1984) 449.

[89] G. M. Batanov: Sov. Phys.-Solid State **3** (1961) 409.

[90] L. A. Dietz: Rev. Sci. Instrum. **36** (1965) 1763.

[91] J. D. Stein and F. A. White: J. Appl. Phys. **43** (1972) 2617.

[92] J. F. Ziegler, J. P. Biersack and U. Littmark: *The Stopping and Range of Ions in Solids*, ed. J. F. Ziegler, (Pergamon Press, New York, 1985) Chap. 4, p. 109.

[93] W.-K. Chu, J. W. Mayer and M.-A. Nicolet: *Backscattering Spectrometry* (Academic Press, Inc., Orlando, 1978) Chap. 2, p. 44.

[94] J. Ishikawa: *Iongen Kougaku* (Ion Source Engineering) (Ionics, Tokyo, 1978) 1st ed., Chap. 2, p. 28 [in Japanese].

[95] T. E. Everhart, N. Saeki, R. Shimizu and T. Koshikawa: J. Appl. Phys. **47** (1976) 2941.

[96] T. Koshikawa and R. Shimizu: J. Phys. D: Appl. Phys. **6** (1973) 1369.

[97] H. Tsuji, J. Ishikawa, T. Maekawa and T. Takagi: Nucl. Instrum. & Methods Phys. Res. **B37/38** (1989) 231.

[98] J. Ishikawa, H. Tsuji and T. Maekawa: Vacuum **39** (1989) 1127.

[99] S. Chikazumi, K. Kigoshi and S. Tanuma: *Revision the Newest Chemical Element Data* (Kaitei Saishin Genso Chishiki) (Tokyo-Shoseki, Tokyo, 1985) 1st ed.

[100] N. A. Surplice and R. J. D'Arcy: J. Phys. E: Sci. Instrum. **3** (1970) 477.

[101] S. Sakai, Y. Gotoh, H. Tsuji, Y. Toyota, J. Ishikawa, M. Tanjyo and K. Matsuda: Nucl. Instrum. & Methods Phys. Res. **B96** (1995) 43.

[102] B. Feuerbacher and B. Fitton: J. Appl. Phys. **43** (1972) 1563.

[103] P. Nye and A. Dinnis: Scanning **7** (1985) 117.

[104] W. G. Durrer, M. Portillo, P. Wang and D. P. Russell: Appl. Surf. Sci. **81** (1994) 215.

[105] P. J. Møller and J. He: Nucl. Instrum. & Methods Phys. Res. **B17** (1986) 137.

[106] J. Cazaux, K. H. Kim, O. Jbara and G. Salace: J. Appl. Phys. **70** (1991) 960.

[107] P. A. Wolff: Phys. Rev. **95** (1954) 56.

List of Publications

Full length papers and letters

[1] H. Tsuji, S. Sakai, Y. Okayama, Y. Toyota, Y. Gotoh, M. Tanjyo, K. Matsuda, and J. Ishikawa:
"Negative-ion current density dependence of the surface potential of insulated electrode during negative-ion implantation",
J. Vac. Soc. Jpn. **37** (1994) pp. 135–138 [in Japanese].

[2] H. Tsuji, Y. Toyota, S. Nagumo, Y. Gotoh, J. Ishikawa, S. Sakai, M. Tanjyo, and K. Matsuda:
"Surface potential measurement of the insulator with secondary electron caused by negative ion implantation",
J. Vac. Soc. Jpn. **37** (1994) pp. 139–142 [in Japanese].

[3] J. Ishikawa, H. Tsuji, Y. Toyota, Y. Gotoh, K. Matsuda, M. Tanjyo, and S. Sakai:
"Negative-ion implantation technique",
Nucl. Instrum. & Methods Phys. Res. **B96** (1995) pp. 7–12.

[4] H. Tsuji, S. Nagumo, Y. Toyota, Y. Gotoh, J. Ishikawa:
"Charging potential measurement of photoresist-layer surface during negative-ion implantation from ion-induced secondary electron energy analysis",
J. Vac. Soc. Jpn. **38** (1995) pp. 221–223 [in Japanese].

[5] Y. Toyota, H. Tsuji, S. Nagumo, S. Sakai, Y. Gotoh, J. Ishikawa, and K. Matsuda:
"Evaluation of charging model in negative-ion implantation",
J. Vac. Soc. Jpn. **38** (1995) pp. 224–227 [in Japanese].

[6] Y. Toyota, H. Honda, H. Tsuji, Y. Gotoh, and J. Ishikawa:
"Energy distribution and yield of secondary electrons emitted from insulator during negative-ion implantation",
J. Vac. Soc. Jpn. **38** (1995) p. 796 [in Japanese].

[7] Y. Toyota, H. Tsuji, Y. Gotoh, and J. Ishikawa:
"Energy distribution and yield measurement of secondary electrons to evaluate the equilibrium charging voltage of an isolated electrode during negative-ion implantation",
Jpn. J. Appl. Phys. **34** (1995) pp. 6487–6491.

[8] Y. Toyota, H. Tsuji, S. Nagumo, Y. Gotoh, and J. Ishikawa:

"Charging phenomenon of insulators in negative-ion implantation",
to be published in Appl. Surf. Sci.

[9] Y. Toyota, H. Tsuji, Y. Gotoh, and J. Ishikawa:
"Yield measurement of secondary electrons emitted from silicon dioxide film in negative-ion bombardment",
submitted to Jpn. J. Appl. Phys.

Proceedings

[1] Y. Toyota, Y. Okayama, H. Tsuji, Y. Gotoh, J. Ishikawa, S. Sakai, M. Tanjyo, K. Matsuda:
"Surface potential versus current density characteristics in negative ion implantation into insulated silicon substrate",
Proc. 4th Symp. Beam Engineering of Advanced Material Syntheses, Tokyo, 1993 (Ionics, Tokyo, 1993) pp. 75-78 [in Japanese].

[2] S. Nagumo, Y. Toyota, H. Tsuji, Y. Gotoh, J. Ishikawa, S. Sakai, M. Tanjyo, and K. Matsuda:
"Surface potential measurement of insulators in negative-ion implantation by secondary electron energy-peak shift",
Proc. 4th Symp. Beam Engineering of Advanced Material Syntheses, Tokyo, 1993 (Ionics, Tokyo, 1993) pp. 79-82 [in Japanese].

[3] H. Tsuji, Y. Toyota, J. Ishikawa, S. Sakai, Y. Okayama, S. Nagumo, Y. Gotoh, and K. Matsuda:
"Charging voltage measurement of an isolated electrode and insulators during negative-ion implantation",
Proc. 10th Int. Conf. Ion Implantation Technology, Catania, 1994 (North-Holland, Amsterdam, 1995) pp. 612-615.

[4] Y. Toyota, H. Tsuji, S. Nagumo, C. Ichihara, S. Sakai, Y. Gotoh, and J. Ishikawa:
"Charging voltage model and its experimental evaluation of isolated electrode in negative-ion implantation",
Proc. 5th Symp. Beam Engineering of Advanced Material Syntheses, Tokyo, 1994 (Ionics, Tokyo, 1994) pp. 209-212 [in Japanese].

[5] S. Ikeda, Y. Toyota, H. Tsuji, Y. Gotoh, and J. Ishikawa:
"Measurement of secondary electrons emitted in negative-ion implantation",
Proc. 6th Symp. Beam Engineering of Advanced Material Syntheses, Tokyo, 1995 (Ionics, Tokyo, 1995) pp. 175-178 [in Japanese].